
Self-Guided Diffusion Model for Accelerating Computational Fluid Dynamics

Ruoyan Li^{1,*}, Zijie Huang^{1,*}, Haixin Wang¹, Guancheng Wan¹, Yizhou Sun¹, Wei Wang^{1,†}

¹University of California, Los Angeles

liruoyan2002@g.ucla.edu

Abstract

Machine learning methods, such as diffusion models, are widely explored as a promising way to accelerate high-fidelity fluid dynamics computation via a super-resolution process from faster-to-compute low-fidelity input. However, existing approaches usually make impractical assumptions that the low-fidelity data is down-sampled from high-fidelity data. In reality, low-fidelity data is produced by numerical solvers that use a coarser resolution. Solver-generated low-fidelity data usually sacrifices fine-grained details, such as small-scale vortices compared to high-fidelity ones. Our findings show that SOTA diffusion models struggle to reconstruct fine-scale details when faced with solver-generated low-fidelity inputs. To bridge this gap, we propose SG-Diff, a novel diffusion model for reconstruction, where both low-fidelity inputs and high-fidelity targets are generated from numerical solvers. We propose an *Importance Weight* strategy during training that serves as a form of self-guidance, focusing on intricate fluid details, and a *Predictor-Corrector-Advancer* SDE solver that embeds physical guidance into the diffusion sampling process. Together, these techniques steer the diffusion model toward more accurate reconstructions. Experimental results on four 2D turbulent flow datasets demonstrate the efficacy of SG-Diff against state-of-the-art baselines.

1 Introduction

High-fidelity simulations of computational fluid dynamics (CFD) are crucial for understanding fluid interactions in engineering systems, greatly impacting design and application outcomes (Wang et al., 2024). Traditional approaches such as Direct Numerical Simulation (DNS) offer high-resolution solutions. However, they are computationally expensive, especially for turbulence with high Reynolds numbers (Zhang et al., 2023). Therefore, learning neural-based simulators from data becomes an attractive alternative, balancing between efficiency and simulation fidelity (Huang et al., 2023).

One popular strategy is to reconstruct high-fidelity data from low-fidelity inputs, where the input data usually reduces the discretization grid size in the spatial domain and thus is computational-efficient (Shu et al., 2023; Pradhan & Duraisamy, 2021). Various machine learning models, including those based on Convolutional Neural Networks (CNNs) (Fukami et al., 2019), Generative Adversarial Networks (GANs) (Li & McComb, 2022), and Diffusion Models (Shu et al., 2023; Shan et al., 2024), have been developed to reconstruct high-fidelity CFD data from low-fidelity inputs. The majority of them are categorized as direct mapping models, which require both low- and high-fidelity data for training and can only capture a particular resolution mapping. In contrast, diffusion models (Shu et al., 2023) only require high-fidelity data during training and use low-fidelity data as intermediate samples in the denoising (inference) stage as guidance for reconstruction. Therefore, they can reconstruct from low-fidelity data at any resolution without retraining and are particularly useful when large-scale solver-generated low-fidelity data are unavailable.

*Equal contribution. †Corresponding author.

One fundamental drawback in existing models is that low-fidelity data is artificially downsampled from high-fidelity data at the same timestamp. Such data inherently has more information compared to solver-generated low-fidelity data in reality, where coarser discretization grids are used in numerical solvers to save computational resources. As illustrated in Figure 1, the former follows “integrate then downsample”, which starts from the high-fidelity initial states to rollout trajectories, and then downsample at each timestamp. The latter follows “downsample then integrate”, which downsamples the high-fidelity initial state to obtain coarser discretization grids as starting points and rollout trajectories through numerical solvers.

Sarkar et al. (2023) evaluate direct mapping models that are trained and tested on solver-generated low-fidelity data. These approaches depend on large collections of low- and high-fidelity pairs from numerical solvers for training, and degrade once the low-fidelity inputs deviate from their training distribution. In reality, large-scale solver-generated low- and high-fidelity pairs are often unavailable (Shu et al., 2023). As a result, **we study how to use diffusion model for reconstructing high-fidelity CFD data from solver-generated low-fidelity data when large-scale solver-generated low- and high-fidelity data pairs are unavailable for training.** Our experiments reveal that SOTA diffusion models struggle to recover fine-grained high-fidelity details given solver-generated low-fidelity inputs, and we show why they fail. In response to this challenge, we build upon the state-of-the-art model proposed by Shu et al. (2023) and propose an *Importance Weight* strategy during training as self-guidance to locate fine-grained high-fidelity details, and a *Predictor-Corrector-Advancer* stochastic differential equation (SDE) solver during inference for ensuring physical consistency. The two modules jointly guide the diffusion model toward higher-quality reconstructions.

Our key contributions are summarized as follows:

- **Problem Identification.** We study a novel problem on reconstructing high-fidelity flow fields with solver-generated low-fidelity data when large-scale solver-generated low-fidelity data are unavailable for training. Our evidence reveals that SOTA diffusion models fail to generate high-quality outputs due to the loss of fine-grained detail in low-fidelity data.
- **Practical Solution.** In light of this issue, we propose SG-Diff, a novel diffusion model with *Importance Weight* strategy during training as self-guidance and a *Predictor-Corrector-Advancer* SDE solver for physically coherent sampling.
- **Experimental Validation.** We present empirical evidence of SG-Diff’s superior performance in a variety of 2D turbulent flow over 4 datasets. It yields a significant improvement in terms of predictive accuracy, physical consistency, and perceptual quality.

2 Preliminaries and Related Work

We consider a machine learning model $f_\theta : \mathcal{X} \rightarrow \mathcal{Y}$ with parameters θ , which transforms a data sample from low-fidelity domain $x \in \mathcal{X} \subseteq \mathbb{R}^{m \times m}$ to high-fidelity domain $y \in \mathcal{Y} \subseteq \mathbb{R}^{n \times n}$ ($m < n$). The distributions of the training and test sets for low-fidelity data are denoted by $p_{\mathcal{X}}^{\text{train}}$ and $p_{\mathcal{X}}^{\text{test}}$, respectively, and for high-fidelity data as $p_{\mathcal{Y}}^{\text{train}}$ and $p_{\mathcal{Y}}^{\text{test}}$. The objective is to develop f_θ such that it can effectively map samples from $\mathcal{X}^{\text{test}}$ to their corresponding high-fidelity counterparts $\mathcal{Y}^{\text{test}}$. As diffusion model operates on the same input and output grid, we upsample the low-fidelity data uniformly during inference as the model input.

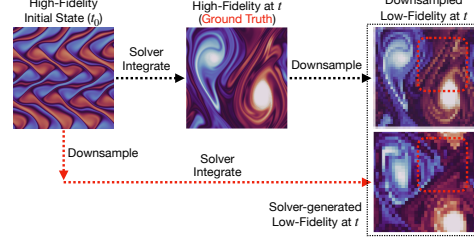


Figure 1: Comparison between downsampled (**black** line) and solver-generated (**red** line) flow fields. Solver-generated low-fidelity data retain less information, especially for fine-grained high-fidelity details.

²For direct mapping models, the training takes low- and high-fidelity pairs as inputs. For diffusion models such as Shu et al. (2023), the training only requires high-fidelity data, and low-fidelity data is used as input during testing.

2.1 AI for Computational Fluid Dynamics (CFD)

Recent advances in machine learning have led to various learning-based surrogate models for accelerating scientific discoveries (Sanchez-Gonzalez et al., 2020; Li et al., 2020, 2021). In the field of high-fidelity CFD reconstruction, researchers have developed powerful models rooted in image super-resolution domain in computer vision. For example, Ren et al. (2023); Jiang et al. (2020) leveraged CNN for spatial-temporal super-resolution. Li & McComb (2022) further advanced the field by proposing physics-informed GANs. Additionally, Fu et al. (2023) proposed a refinement network to address the issue with limited high-fidelity data. These models rely on low- and high-fidelity data pairs during training and can only capture specific resolution mappings. As a result, Shu et al. (2023) leveraged diffusion model, which is trained exclusively on high-fidelity data and enables reconstruction from any type of low-fidelity input. However, these methods assume the low-fidelity data is artificially downsampled from high-fidelity sources, which limits their performance during inference when reconstructing from solver-generated low-fidelity data.

2.2 Diffusion Model

Diffusion models have become a prominent class of deep generative models, demonstrating state-of-the-art performance across various domains such as image generation (Meng et al., 2022; Saharia et al., 2021; Ho et al., 2020; Li et al., 2025), video synthesis (Yang & Hong, 2022; Yu et al., 2022), and applications in scientific fields (Shu et al., 2023; Yang & Sommer, 2023; Qiu et al., 2024). Diffusion models are grounded in a stochastic diffusion process, akin to those found in thermodynamics. It contains a forward and reverse process, where a data sample is gradually corrupted with noise, and a neural network is trained to reverse this. The forward process is defined by the SDE:

$$dx = f(x, t)dt + g(t)dW_t, \quad x_0 \sim p_{\text{data}}(x), \quad (1)$$

where $f(x, t)$ is the drift function, $g(t)$ is a time-dependent diffusion coefficient, and dW_t is Brownian motion. $t \in [0, T]$ is a continuous time variable with $t = 0$ corresponding to original data and $t = T$ corresponding to pure noise. The reverse diffusion is given by

$$dx = [f(x, t) - g(t)^2 \nabla_x \log p_t(x)] dt + g(t)d\bar{W}_t, \quad (2)$$

where $\nabla_x \log p_t(x)$ is the score function of the intractable marginal distribution and $d\bar{W}_t$ is the reverse-time Brownian motion. We leverage a parametrized score model $s_\theta(x_t, t)$ to estimate the score function and use the score matching objective (Song et al., 2021) for training:

$$\mathbb{E}_{t, x_0, x_t} [\lambda(t) \|s_\theta(x_t, t) - \nabla_{x_t} \log p_t(x_t | x_0)\|^2], \quad (3)$$

where $t \sim \text{Uniform}(0, T)$ and $x_t \sim p(x_t | x_0)$.

3 Method:SG-Diff

We build upon the diffusion framework proposed by Shu et al. (2023) and study reconstructing high-fidelity data from solver-generated low-fidelity inputs, which have more information loss compared to artificially downsampled low-fidelity inputs. Our model, SG-Diff, features an *Importance Weight* strategy that scores different components in the flow fields through the loss function in a self-supervised manner, forcing the model to recover more fine-grained high-fidelity details during training. In addition, a *Predictor-Corrector-Advancer* SDE solver applies physics-informed correction during sampling, ensuring physical coherence in reconstructed samples during inference. The two modules jointly guide the model toward high-quality reconstruction from a wide range of low-fidelity inputs. The overall framework is depicted in Figure 2. We now introduce each component in detail.

Model Setup. SG-Diff follows the guided data synthesis setting as in Shu et al. (2023); Meng et al. (2022): we train the model with high-fidelity sources only, and condition on low-fidelity inputs as intermediate diffusion step during inference. This brings two benefits: (1) exerting control over the reconstruction process during inference. Instead of starting from random noises, the reverse diffusion starts from low-fidelity inputs as intermediate diffusion steps. (2) The model can reconstruct from generalized low-fidelity data, since the training does not depend on low- and high-fidelity pairs as in direct mapping models such as CNNs.

Formally, during the forward training process, we obtain intermediate diffusion states x_t by solving the following forward SDE. We adopt VP-SDE (Ho et al., 2020), where $f(x, t) = -\frac{1}{2}\beta_t x_t$, $g(t) = \sqrt{\beta_t}$,

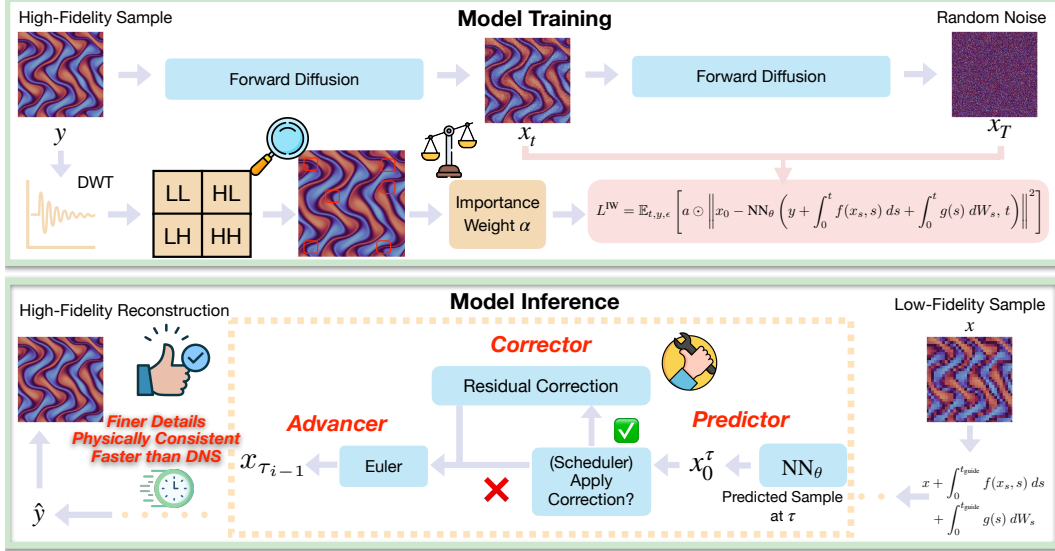


Figure 2: Training and inference pipeline of SG-Diff. Training with high-fidelity data only, guided by Importance Weight strategy to locate fine-grained high-fidelity details. During inference, low-fidelity data is used as guidance, and the Predictor-Corrector-Advancer solver ensures physical coherence.

and $\{\beta_1, \dots, \beta_T\}$ are variance schedules. The forward procedure continuously adds noises to the high-fidelity sample x_0 .

$$dx_t = f(x_t, t)dt + g(t)dW_t, \quad x_0 = y \sim p_{\mathcal{Y}}^{\text{train}}. \quad (4)$$

During inference stage, instead of starting from $x_T \sim N(0, I)$, we obtain the intermediate diffusion state $x_{t_{\text{guide}}}$ ($0 < t_{\text{guide}} < T$) by adding noises to the conditioned low-fidelity data $x \sim p_{\mathcal{X}}^{\text{test}}$ as

$$x_{t_{\text{guide}}} = x + \int_0^{t_{\text{guide}}} f(x_s, s) ds + \int_0^{t_{\text{guide}}} g(s) dW_s. \quad (5)$$

We adopt the same t_{guide} as Shu et al. (2023), and use $x_{t_{\text{guide}}}$ as the starting point for the reverse process to reconstruct the high-fidelity sources. Then, we solve the reverse SDE in Equation 2 to progressively produce a refined high-fidelity reconstruction that aligns with the low-fidelity conditioning data. Shu et al. (2023) applied the above procedure to reconstruct high-fidelity data from artificially downsampled low-fidelity input. We demonstrate in Proposition 3.1 why their proposed diffusion model performs poorly for solver-generated low-fidelity data. For solver-generated low-fidelity data, the differences in noised probability distributions become larger, which hinders diffusion model's ability for accurate reconstruction. We show the detailed proof in Appendix J.

Proposition 3.1. *Let $p_{\mathcal{Y}}$ denote the probability distribution of high-fidelity data. Let $p_{\mathcal{X}}$ and $q_{\mathcal{X}}$ denote the probability distribution of solver generated and downsampled low-fidelity data respectively. Define $\tilde{p}_{\mathcal{Y}}$, $\tilde{p}_{\mathcal{X}}$, and $\tilde{q}_{\mathcal{X}}$ to be the probability distribution transformed from $p_{\mathcal{Y}}$, $p_{\mathcal{X}}$, and $q_{\mathcal{X}}$ by applying Equation 5. Then, it follows that $D_{\text{KL}}(\tilde{p}_{\mathcal{Y}} \parallel \tilde{p}_{\mathcal{X}}) \geq D_{\text{KL}}(\tilde{p}_{\mathcal{Y}} \parallel \tilde{q}_{\mathcal{X}})$.*

3.1 Importance Weight During Training

We therefore introduce an importance weighting mechanism during training as self-guidance to ensure accurate reconstruction of fine-grained details. Specifically, we transform the high-fidelity data into the wavelet domain using the DWT and assign importance scores to different components of fluid fields within the diffusion loss function. By considering spatial relationships between nearby vorticity, DWT has great abilities to locate information both in spatial and frequency domains (Daubechies, 1992; Akansu & Haddad, 1992), thus allowing the model to capture fine-grained structures effectively. Formally, we decompose fluid fields $y \in \mathcal{R}^{n \times n}$ into frequency subdomains and compute the sum of

squares of the high-frequency modes – namely HL (high-low), LH (low-high) and HH (high-high) subdomains as below, where $HL, LH, HH, F \in \mathbb{R}^{\frac{n}{2} \times \frac{n}{2}}$. HL captures horizontal high-frequency signals, while LH captures vertical high-frequency signals. HH captures high-frequency signals in both directions, corresponding to diagonal details such as intersections.

$$F = HL^2 + LH^2 + HH^2. \quad (6)$$

To compute importance scores, we then uniformly upsample F to $\hat{F} \in \mathbb{R}^{n \times n}$ and linearly map $\hat{F}_{i,j}$ to an importance weight $a_{i,j}$ as below, where α, β are the minimum and maximum importance weight value respectively, $Q_\theta(\hat{F}) \in \mathbb{R}$ is the θ quantile of all \hat{F} values.

$$a_{i,j} = \begin{cases} \alpha + (\beta - \alpha) \frac{\hat{F}_{i,j} - Q_\theta(\hat{F})}{\max \hat{F} - Q_\theta(\hat{F})} & \text{if } \hat{F}_{i,j} > Q_\theta(\hat{F}) \\ 1 & \text{otherwise} \end{cases} \quad (7)$$

If $\hat{F}_{i,j}$ exceeds the θ quantile of all \hat{F} values, the corresponding component is considered high-frequency, and will be assigned with weight greater than 1. Finally, the diffusion loss function in Eqn 3 is updated to incorporate the importance weighting. Note that our diffusion models directly predict the denoised sample instead of noise or score.

$$L^{\text{IW}} = \mathbb{E}_{t,y,\epsilon} \left[a \odot \left\| x_0 - \text{NN}_\theta \left(y + \int_0^t f(x_s, s) ds + \int_0^t g(s) dW_s, t \right) \right\|^2 \right], \quad (8)$$

where x_0 represents the ground truth high-fidelity sample, NN_θ predicts the denoised high-fidelity sample, and \odot denotes element-wise multiplication.

Importance Weight Design Choice. Our *importance weight* strategy is incorporated exclusively during training. The DWT-based calculation avoids the large computational complexity often associated with attention mechanisms. It efficiently emphasizes important features by leveraging the intrinsic properties of the wavelet transform, resulting in a more targeted learning process.

3.2 Predictor-Corrector-Advancer SDE Solver

In addition, we introduce a *Predictor-Corrector-Advancer* SDE solver to enhance the physical coherence of the reconstructed data during inference. In the reverse diffusion process, the *Predictor* first generate predicted high-fidelity data $\tilde{x}_0^t = \text{NN}_\theta(x_t, t)$. Then, the *Corrector* applies residual corrections to \tilde{x}_0^t to enhance physical consistency. Let \mathcal{L} be a differential operator associated with a PDE acting on a function $u : \Omega \rightarrow \mathbb{R}^{n \times n}$, defined on a domain $\Omega \subset \mathbb{R}^{n \times n}$, with source term $f : \Omega \rightarrow \mathbb{R}^{n \times n}$. The PDE is expressed as $\mathcal{L}u(x) = f(x)$, $x \in \Omega$. Given an approximate solution $\tilde{u}(x)$, the PDE residual $\mathcal{R}(x)$ is defined as $\mathcal{R}(x) := \|\mathcal{L}\tilde{u}(x) - f(x)\|_2^2$. The correction is to perform M steps gradient descent based on the residuals using the Adam algorithm (Kingma & Ba, 2015). Finally, the *Advancer* leverages Euler–Maruyama (Maruyama, 1955) to advance to the next diffusion step. The inference procedure is summarized in Algorithm 1.

Algorithm 1 Predictor-Corrector-Advancer Inference Algorithm.

Require: $x \in \mathcal{X}^{\text{test}}$, t_{guide} , $\tau = \{\tau_0, \tau_1, \dots, \tau_K\}$ (backward steps, where $\tau_0 = 0, \dots, \tau_K = t_{\text{guide}}$), $\text{NN}_\theta, \mathcal{R}(\cdot)$, M (gradient descent steps), η (step size).

- 1: $x_{\tau_k} = x + \int_0^{\tau_k} f(x_s, s) ds + \int_0^{\tau_k} g(s) dW_s$.
- 2: **for** $i = K, K-1, \dots, 1, 0$ **do**
- 3: *Predictor*: $\tilde{x}_0^{\tau_i} = \text{NN}_\theta(x_{\tau_i}, \tau_i)$
- 4: **if** correction is performed at time τ_{i-1} **then**
- 5: **repeat**
- 6: *Corrector*: $\tilde{x}_0^{\tau_i} = \tilde{x}_0^{\tau_i} - \eta \cdot \text{Adam}(\nabla \mathcal{R}(\tilde{x}_0^{\tau_i}))$
- 7: **until** M times
- 8: **end if**
- 9: *Advancer*: $x_{\tau_{i-1}} = x_{\tau_i} + \left[f(x_{\tau_i}, \tau_i) + g^2(\tau_i) \frac{x_{\tau_i} - \tilde{x}_0^{\tau_i} - \int_0^{\tau_i} f(x_s, s) ds}{\int_0^{\tau_i} g^2(s) dW_s} \right] dt + g(t) d\bar{W}_{\tau_i}$
- 10: **end for**

We begin by analyzing the convergence properties of the *Corrector*. Proposition 3.2 suggests that increasing the number of gradient descent steps leads to a smaller residual $\mathcal{R}(x)$. Thus, for optimal physical consistency, Proposition 3.2 suggests to perform more gradient descent steps, i.e. larger M .

Proposition 3.2 (Convergency of *Corrector* (Kingma & Ba (2015) Corollary 4.2)). *Define the regret $r(M) = \sum_{i=1}^M [\mathcal{R}(x_i) - \mathcal{R}(x^*)]$, where $x^* = \operatorname{argmin}_x \sum_{i=1}^M \mathcal{R}(x)$. Assume $\mathcal{R}(x)$ has bounded gradient and distance between any x_i generated by Adam is bounded. The *Corrector* achieves the following guarantee, for all $M \geq 1$: $\frac{r(M)}{M} = O\left(\frac{1}{\sqrt{M}}\right)$.*

We then introduce the error bound for our *Predictor-Corrector-Advancer* SDE solver in Proposition 3.3, with proof detailed in Appendix K. The derived bound indicates that, under finite temporal discretization Δt , (1) an increase in the correction region, $|A|$, could lead to an increase in the prediction error; and (2) a higher number of gradient descent steps, M , similarly could result in larger predictive error. This observation is noteworthy because, while Proposition 3.2 demonstrates that a larger M enhances the physical consistency, Proposition 3.3 simultaneously reveals that it adversely affects predictive accuracy. Consequently, these findings highlight the importance of balancing the competing influences of physical consistency and prediction accuracy. To address such trade-off, Section 4.4 investigates into (1) determining an optimal schedule for applying the correction; and (2) establishing the optimal frequency of correction.

Proposition 3.3 (Error Bound for *Predictor-Corrector-Advancer*). *Let \hat{x}_t denotes the piecewise solution of x_t solved using the *Predictor-Corrector-Advancer* method. Then,*

$$Z(T) = \sup_{0 \leq s \leq T} \mathbb{E} [|x_s - \hat{x}_s|^2] \leq O(\Delta t \exp(O(|A|^2(1 + \eta L_Q L_{\mathcal{R}})^{2M}))), \quad (9)$$

where $\eta, L_Q, L_{\mathcal{R}}$ are positive constant. A denotes the region where correction is applied and B otherwise. $A \cup B = [0, T]$ and $A \cap B = \emptyset$.

Additionally, we notice that the expected error approaches zero as the time discretization Δt approaches zero. This implies the strong and weak convergency of our method.

Proposition 3.4 (Strong and Weak Convergency of *Predictor-Corrector-Advancer* SDE Solver). *The SDE solver outlined in Algorithm 1 satisfies both strong and weak convergency. Namely, for any appropriate test function ϕ .*

$$\lim_{\Delta t \rightarrow 0} \sup_{0 \leq s \leq T} \mathbb{E} [|x_s - \hat{x}_s|^2] = 0 \quad (\text{Strong Convergency}) \quad (10)$$

$$\lim_{\Delta t \rightarrow 0} |\mathbb{E} [\phi(\hat{x}_{t_N})] - \mathbb{E} [\phi(x_T)]| = 0 \quad (\text{Weak Convergency}) \quad (11)$$

The strong convergency implies the sample paths of the numerical approximation approach those of the true process in a mean sense. Equivalently, the error measured pathwise becomes arbitrarily small. Weak convergency is a result of strong convergency, and it guarantees the target distributions of the approximations converge.

Huang et al. (2024) and Bastek et al. (2025) also embed PDE residuals in diffusion models. The former injects the residual's gradient into the score, while the latter adds the residual to the loss function. We instead apply several Adam updates to the predicted clean sample at selected reverse-diffusion steps, analytically establishing both the accuracy and physical consistency trade-off and the method's convergence. For comparison, we combine the residual score guidance of Huang et al. (2024) with the vanilla model of Shu et al. (2023) to create a Residual Score-Guided Diffusion (RSGD) baseline and also include the residual-loss approach of Shan et al. (2024) during experiments.

3.3 Connection to Diffusion Posterior Sampling

Diffusion models have shown great performance in image super-resolution tasks (Zhu et al., 2023; Chung et al., 2023; Rozet & Louppe, 2023; Kawar et al., 2022). These studies assume that for high-fidelity data y and low-fidelity data x , there exists \mathcal{A} such that $x = \mathcal{A}(y) + \epsilon$, where ϵ is random noise. While this holds for straightforward downsampling, our solver-generated low-fidelity data can only approximate by $\mathcal{A}(y) \approx \text{ForwardSolver}(\text{Downsample}(\text{ReverseSolver}(y, t_{\text{fluid}})), t_{\text{fluid}})$. $\text{ReverseSolver}(y, t_{\text{fluid}})$ integrates backward to estimate the initial high-fidelity state, which is downsampled and used by ForwardSolver to produce the low-fidelity data. Computing gradients with respect to \mathcal{A} is impractical due to adaptive time stepping resulting in tens of thousands iterations for numerical solvers. As a result, previous approaches cannot be directly applied, but we still

include some as baselines due to their prominence in related tasks. In our experiments, we adopt a downsampling strategy for \mathcal{A} following Chung et al. (2023).

To incorporate low-fidelity data into the reverse diffusion process, we follow Shu et al. (2023) by treating the low-fidelity data as intermediate reverse diffusion samples. We contend that this strategy offers stronger guidance. Although the gradient guidance from previous works facilitates projection onto the measurement subspace, our problem is characterized by a focus on a hard L2 loss, thereby requiring convergency to exact target point. As demonstrated in the experimental section, Zhu et al. (2023); Chung et al. (2023) often produce significantly larger L2 loss.

4 Experiments

4.1 Dataset

We generate four 2D turbulent flow datasets using the incompressible Navier-Stokes: 1.) *Taylor Green Vortex*, featuring gradually break down of large-scale vortices into smaller turbulent structures; 2.) *Decaying Turbulence*, describing turbulence that evolves naturally without external forces; 3.) *Kolmogorov Flow*, portraying turbulence influenced by a sinusoidal external force; 4.) *McWilliams Flow* (Mcwilliams, 1984), describing the behavior of isolated vortices in turbulent conditions.

$$\frac{\partial \omega(\mathbf{x}, t)}{\partial t} + \mathbf{u}(\mathbf{x}, t) \cdot \nabla \omega(\mathbf{x}, t) = \frac{1}{Re} \nabla^2 \omega(\mathbf{x}, t) + f(\mathbf{x}), \quad \nabla \cdot \mathbf{u}(\mathbf{x}, t) = 0, \quad \omega(\mathbf{x}, 0) = \omega_0(\mathbf{x}),$$

where ω represents vorticity, \mathbf{u} denotes velocity field, Re is the Reynolds number, and $f(\mathbf{x})$ is an external forcing. ω_0 represents the initial vorticity distribution. The PDE is numerically solved by pseudo-spectral solver (Orszag, 1972) on equispaced discretization grids. The high-fidelity data are generated with 4096×4096 grid and then uniformly downsampled to 256×256 , while those on the lower-resolution grids are considered low-fidelity. We refer the readers to Appendix C for details.

4.2 Experiment Settings

Task Setup and Baselines. We evaluate two reconstruction settings: $64 \times 64 \rightarrow 256 \times 256$ ($4 \times$ upsampling) and $32 \times 32 \rightarrow 256 \times 256$ ($8 \times$ upsampling). We compare against seven diffusion based reconstruction models: ResShift (Yue et al., 2023), PiRD (Shan et al., 2024), DiffPIR (Zhu et al., 2023), Diffusion Posterior Sampling (DPS) (Chung et al., 2023), Residual Score Guided Diffusion (RSGD) (Huang et al., 2024), Vanilla Diffusion (Diff) and its conditional variant (Cond Diff) from Shu et al. (2023). We perform two ablation studies, namely SG-Diffw/o IW and SG-Diffw/o Cor, where we remove *Importance Weight* and *Predictor-Corrector-Advancer* respectively. The comparisons between direct mapping models are available in Shu et al. (2023) and Appendix D.

Evaluation Metrics. We assess the reconstructed flow fields using L2 norm for measuring the pointwise error and unnormalized residuals $\mathcal{R}(x)$ (Res.) for assessing adherence to the underlying physics. Our study employs unnormalized residuals, in contrast to the normalized residuals reported in Shu et al. (2023). According to Shu et al. (2023), lower residual values indicate enhanced physical consistency. Given that the high-fidelity residuals are also nonzero, we posit that reconstructed samples whose residuals more closely match those of the high-fidelity data are superior. The nonzero residuals observed even in high-fidelity data can be attributed to the inherent approximations in residual computation with downsampled high-fidelity data as well as the irreducible error present in numerical approximation. Detailed high-fidelity residual data are presented in Table 3 in Appendix C.

In addition, we conduct a novel multi-scale evaluation using DWT: we transform the predicted and ground truth flow fields into wavelet space and decompose them into four subdomains: LL, LH, HL, and HH. The LL subdomain captures large-scale, low-frequency information, while LH, HL, and HH encompass higher-frequency details like turbulent structures. By calculating the L2 norm in each subdomain, we gain a comprehensive understanding of the model’s performance across different scales, ensuring accurate reconstruction of both global flow features and fine-scale details.

4.3 Reconstruction Results

Table 1 reports the L2 loss and PDE residual across datasets and models. For both upsampling scales, SG-Diff consistently outperforms baselines, showing its effectiveness. The lower L2 achieved

		DiffPIR	DPS	ResShift	PiRD	RSGD	Diff	Cond Diff	SG-Diff	SG-Diff w/o Cor	SG-Diff w/o IW
<i>Taylor Green Vortex</i>	L2	7.09	7.08	3.57	3.97	4.50	3.28	4.50	3.18	3.20	3.22
	Res.	6115272.05	6115028.67	4047.63	6.65	1918.81	41732.00	1355.17	5308.99	74400.90	6945.75
	L2	6.84	6.83	1.73	2.20	2.53	1.68	3.57	1.55	1.57	1.59
	Res.	6152312.45	6151699.75	3171.31	22.36	442678.57	30626.98	147459.82	4386.29	66705.04	6093.44
<i>Decaying Turbulence</i>	L2	3.89	3.89	1.99	2.00	1.91	1.84	2.02	1.71	1.71	1.72
	Res.	105086.38	105085.79	346.31	8.43	12189.40	9973.20	34853.56	165.48	986.56	284.91
	L2	3.51	3.51	0.93	0.96	0.87	0.85	1.34	0.79	0.81	0.81
	Res.	102022.69	106641.11	345.69	8.45	8055.75	4331.53	15225.19	196.00	1193.32	187.01
<i>Kolmogorov Flow</i>	L2	7.09	7.08	2.90	2.95	3.06	3.09	3.13	2.78	2.82	2.93
	Res.	29717.32	29627.61	494.93	4.32	57.13	180.70	80.62	40.12	668.08	56.64
	L2	7.08	7.07	1.97	1.94	1.75	1.79	1.79	1.61	1.69	1.73
	Res.	29717.33	29624.92	476.34	2.84	94.98	309.98	165.90	39.00	327.20	68.46
<i>McWilliams Flow</i>	L2	4.37	4.36	2.27	2.28	2.33	2.23	2.24	2.04	2.06	2.16
	Res.	1557.96	1554.02	9.23	1.23	11.61	16.09	12.67	5.50	66.00	7.80
	L2	4.36	4.36	1.44	1.43	1.45	1.29	1.30	1.24	1.27	1.30
	Res.	1612.80	1553.69	8.81	1.24	11.94	21.52	31.23	6.36	88.00	12.00

Table 1: Quantitative performance comparison over four datasets on L2 and Res metrics. Rows with a gray background report results for $32 \times 32 \rightarrow 256 \times 256$ tasks, while rows with a white background report results for $64 \times 64 \rightarrow 256 \times 256$ tasks. Columns highlighted in yellow show results for our model and its ablations. **Bold** values indicate the best performance in each row.

by SG-Diff indicates that it effectively captures essential features and dynamics of the turbulent flows. Additionally, residuals from SG-Diff reconstructions are closer to those of the high-fidelity data. The small difference in PDE residuals indicates that SG-Diff’s predictions adhere more closely to the underlying physical laws. For complex datasets dominated by fine-grained details, such as *Kolmogorov Flow* and *McWilliams Flow*, SG-Diff outperforms baselines by a margin, showing better reconstruction accuracy and physical coherence. Through ablation studies, we demonstrate that both *Importance Weight* and *Predictor-Corrector-Advancer* contribute significantly to improving model’s performance, underscoring the effectiveness of our design choices in capturing the complex behaviors of turbulent flows. DiffPIR and DPS have large L2 loss and PDE residual, as expected. This can be attributed to using downsampling to approximate \mathcal{A} and the weaker guidance imposed by these two methods. Although PiRD yields very small PDE residuals for *Taylor-Green Vortex* and *Decaying Turbulence*, these residuals still differ substantially from the high-fidelity reference data. In other words, the method prioritizes reducing the PDE residual at the expense of predictive accuracy, and the smaller residual does not translate into better flow reconstruction.

Multi-Scale Evaluation. We assess the model’s ability to capture flow structures at different scales using DWT. As shown in Appendix E, SG-Diff demonstrates superior performance in all subdomains. Excelling in the LL subdomain indicates a strong capability in capturing large-scale, low-frequency components of the turbulent flows. The superior performance in the LH and HL subdomains suggests the effectiveness of SG-Diff in capturing small-scale vortices and transitions between scales.

Runtime Comparison. We report the runtime comparison of different methods in Appendix G. SG-Diff only increases small inference time while achieving superior performance improvement against baselines. The total runtime of using the numerical solvers to generate low-fidelity data, and reconstructing with SG-Diff is considerably faster than DNS. Note that numerical solvers employs adaptive time stepping governed by Courant–Friedrichs–Lewy (CFL) condition (Courant et al., 1928).

Sensitivity Analysis. We study the effects of three key hyperparameters in calculating the importance weight: the maximum importance weight β , minimum importance weight α , and the threshold parameter θ . The results in Appendix H show that increasing β reduces both L2 and PDE residuals, indicating a broader range of importance weights is beneficial. Smaller α values improve performance while setting α to 1 is suboptimal. This can be understood as it decreases the difference between high-frequency and low-frequency regions, as the weight for the latter one is set to 1. Additionally, a larger θ (0.7 or 0.8) helps the model focus on important details. The experiments presented in Appendix H

are conducted on the validation datasets for *Kolmogorov Flow*. The optimal hyperparameters, selected based on this validation dataset, are applied across all datasets during testing.

Image Similarity Metrics. We also report the Learned Perceptual Image Patch Similarity (LPIPS) score (Zhang et al., 2018), Peak Signal-to-Noise Ratio (PSNR) (Gonzalez & Woods, 2002), and Structural Similarity Index Measure (SSIM) (Wang et al., 2004) in Appendix F. Results show that SG-Diff demonstrate superior performance in these metrics under all settings.

Model Generalization. We observe that SG-Diff generalizes well to low-fidelity data generated with different solver configurations. The experiment results are reported in Appendix I. We generate new *Kolmogorov Flow* datasets by varying solver configurations. We compare our model trained with the original *Kolmogorov Flow* datasets with our model trained directly on the new datasets. Results show that our model trained on the original datasets has comparable performance.

4.4 Physical Guidance

We conduct systematic study on how to schedule the corrector. The experiments are conducted on the validation datasets for *Kolmogorov Flow*. The optimal hyperparameters, selected based on this validation dataset, are applied across all datasets during testing.

Scheduling Policy. We first explore the optimal schedule policy by comparing: 1.) *Uniform N*: Distributing N residual correction steps evenly across diffusion steps; 2.) *Start I, End N* Placing I consecutive correction steps at the start and N at the end of the diffusion process; 3.) *Start N, Space S*: Placing N correction steps at the start with a spacing of S ; 4.) *End N, Space S*: Placing N correction steps at the end with a spacing of S . Results in Table 2 suggest that applying correction steps at the beginning achieves the lowest L2, while applying at the end has the lowest PDE residuals. To balance between L2 and PDE residual, we adopt the *Start N End N* schedule.

Number of Correction Steps. We vary the number of N in the *Start N, End N* policy as shown in Figure 3. We observe that increasing N leads to enhanced physical coherence measured by PDE residuals. However, L2 does not continuously decrease with larger N . It reaches a minimum when $N = 2$. This suggests that while more correction steps improve models’ adherence to physical laws, an excessive number may interfere with the model’s ability to accurately capture the intricate details of the turbulent flow. Therefore, we use *Start 2, End 2* as the optimal balance.

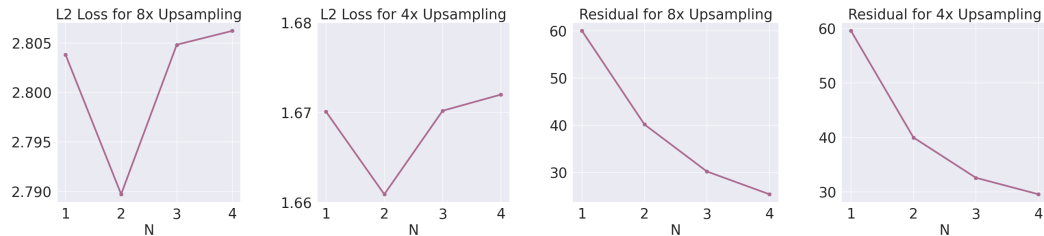


Figure 3: Varying number of N using the *Start N, End N* correction schedule on the *Kolmogorov Flow* dataset. Showing both L2 and Residual across upsampling settings.

5 Conclusion

We study a novel problem of reconstructing high-fidelity CFD from solver-generated low-fidelity inputs. Our diffusion model, SG-Diff, achieves high-quality reconstruction guided by *Importance Weight* and *Predictor-Corrector-Advancer* solver.

References

Akansu, A. N. and Haddad, R. A. *Multiresolution Signal Decomposition: Transforms, Subbands, and Wavelets*. Academic Press, San Diego, CA, 1992.

Bastek, J.-H., Sun, W., and Kochmann, D. Physics-informed diffusion models. In *The Thirteenth International Conference on Learning Representations*, 2025. URL <https://openreview.net/forum?id=tpYeermigp>.

Chung, H., Kim, J., Mccann, M. T., Klasky, M. L., and Ye, J. C. Diffusion posterior sampling for general noisy inverse problems. In *The Eleventh International Conference on Learning Representations*, 2023. URL <https://openreview.net/forum?id=0nD9zGAGT0k>.

Courant, R., Friedrichs, K., and Lewy, H. Über die partiellen differenzengleichungen der mathematischen physik. *Mathematische Annalen*, 100(1):32–74, 1928.

Daubechies, I. *Ten Lectures on Wavelets*. SIAM, Philadelphia, PA, 1992.

Fu, C., Helwig, J., and Ji, S. Semi-supervised learning for high-fidelity fluid flow reconstruction. In *The Second Learning on Graphs Conference*, 2023. URL <https://openreview.net/forum?id=695TYJh1Ba>.

Fukami, K., Fukagata, K., and Taira, K. Super-resolution reconstruction of turbulent flows with machine learning. *Journal of Fluid Mechanics*, 870:106–120, 2019. doi: 10.1017/jfm.2019.238.

Gonzalez, R. C. and Woods, R. E. *Digital Image Processing*. Prentice Hall, 2nd edition, 2002.

Ho, J., Jain, A., and Abbeel, P. Denoising diffusion probabilistic models. *arXiv preprint arxiv:2006.11239*, 2020.

Huang, J., Yang, G., Wang, Z., and Park, J. J. Diffusionpde: Generative pde-solving under partial observation, 2024. URL <https://arxiv.org/abs/2406.17763>.

Huang, Z., Sun, Y., and Wang, W. Generalizing graph ode for learning complex system dynamics across environments. In *Proceedings of the 29th ACM SIGKDD Conference on Knowledge Discovery and Data Mining*, pp. 798–809, 2023.

Jiang, C. M., Esmaeilzadeh, S., Azizzadenesheli, K., Kashinath, K., Mustafa, M. A., Tchelepi, H. A., Marcus, P. S., Prabhat, and Anandkumar, A. Meshfreeflownet: A physics-constrained deep continuous space-time super-resolution framework. *SC20: International Conference for High Performance Computing, Networking, Storage and Analysis*, pp. 1–15, 2020. URL <https://api.semanticscholar.org/CorpusID:218487006>.

Kawar, B., Elad, M., Ermon, S., and Song, J. Denoising diffusion restoration models. In *Advances in Neural Information Processing Systems*, 2022.

Kingma, D. P. and Ba, J. Adam: A method for stochastic optimization. *International Conference on Learning Representations (ICLR)*, 2015. URL <https://arxiv.org/abs/1412.6980>.

Li, M. and McComb, C. Using Physics-Informed Generative Adversarial Networks to Perform Super-Resolution for Multiphase Fluid Simulations. *Journal of Computing and Information Science in Engineering*, 22(4):044501, 02 2022. ISSN 1530-9827. doi: 10.1115/1.4053671. URL <https://doi.org/10.1115/1.4053671>.

Li, R., Sahu, D. R., den Broeck, G. V., and Zeng, Z. Deep generative models with hard linear equality constraints, 2025. URL <https://arxiv.org/abs/2502.05416>.

Li, Z.-Y., Kovachki, N. B., Azizzadenesheli, K., Liu, B., Bhattacharya, K., Stuart, A. M., and Anandkumar, A. Fourier neural operator for parametric partial differential equations. *ArXiv*, abs/2010.08895, 2020. URL <https://api.semanticscholar.org/CorpusID:224705257>.

Li, Z.-Y., Zheng, H., Kovachki, N. B., Jin, D., Chen, H., Liu, B., Azizzadenesheli, K., and Anandkumar, A. Physics-informed neural operator for learning partial differential equations. *ArXiv*, abs/2111.03794, 2021. URL <https://api.semanticscholar.org/CorpusID:243847513>.

Lu, C., Zhou, Y., Bao, F., Chen, J., Li, C., and Zhu, J. Dpm-solver: A fast ode solver for diffusion probabilistic model sampling in around 10 steps. *arXiv preprint arXiv:2206.00927*, 2022.

Maruyama, G. Continuous markov processes and stochastic equations. *Rendiconti del Circolo Matematico di Palermo*, 4:48–90, 1955.

Mcwilliams, J. C. The emergence of isolated coherent vortices in turbulent flow. *Journal of Fluid Mechanics*, 146:21–43, 1984. doi: 10.1017/S0022112084001750.

Meng, C., He, Y., Song, Y., Song, J., Wu, J., Zhu, J.-Y., and Ermon, S. SDEdit: Guided image synthesis and editing with stochastic differential equations. In *International Conference on Learning Representations*, 2022.

Orszag, S. A. Comparison of pseudospectral and spectral approximation. *Studies in Applied Mathematics*, 51(3):253–259, September 1972. doi: 10.1002/sapm1972513253.

Pradhan, A. and Duraisamy, K. Variational multi-scale super-resolution : A data-driven approach for reconstruction and predictive modeling of unresolved physics, 2021. URL <https://arxiv.org/abs/2101.09839>.

Qiu, J., Huang, J., Zhang, X., Lin, Z., Pan, M., Liu, Z., and Miao, F. Pi-fusion: Physics-informed diffusion model for learning fluid dynamics, 2024. URL <https://arxiv.org/abs/2406.03711>.

Ren, P., Rao, C., Liu, Y., Ma, Z., Wang, Q., Wang, J.-X., and Sun, H. Physr: Physics-informed deep super-resolution for spatiotemporal data. *Journal of Computational Physics*, 492:112438, 2023. ISSN 0021-9991. doi: <https://doi.org/10.1016/j.jcp.2023.112438>. URL <https://www.sciencedirect.com/science/article/pii/S0021999123005338>.

Rozet, F. and Louppe, G. Score-based data assimilation. In *Thirty-seventh Conference on Neural Information Processing Systems*, 2023. URL <https://openreview.net/forum?id=VUvLSnMZdX>.

Saharia, C., Ho, J., Chan, W., Salimans, T., Fleet, D. J., and Norouzi, M. Image super-resolution via iterative refinement. *arXiv:2104.07636*, 2021.

Sanchez-Gonzalez, A., Godwin, J., Pfaff, T., Ying, R., Leskovec, J., and Battaglia, P. Learning to simulate complex physics with graph networks. In III, H. D. and Singh, A. (eds.), *Proceedings of the 37th International Conference on Machine Learning*, volume 119 of *Proceedings of Machine Learning Research*, pp. 8459–8468. PMLR, 13–18 Jul 2020. URL <https://proceedings.mlr.press/v119/sanchez-gonzalez20a.html>.

Sarkar, R. K., Majumdar, R., Jadhav, V., Sakhinana, S. S., and Runkana, V. Redefining super-resolution: Fine-mesh pde predictions without classical simulations, 2023. URL <https://arxiv.org/abs/2311.09740>.

Shan, S., Wang, P., Chen, S., Liu, J., Xu, C., and Cai, S. Pird: Physics-informed residual diffusion for flow field reconstruction, 2024. URL <https://arxiv.org/abs/2404.08412>.

Shu, D., Li, Z., and Farimani, A. B. A physics-informed diffusion model for high-fidelity flow field reconstruction. *Journal of Computational Physics*, pp. 111972, 2023.

Song, Y., Sohl-Dickstein, J., Kingma, D. P., Kumar, A., Ermon, S., and Poole, B. Score-based generative modeling through stochastic differential equations. In *International Conference on Learning Representations*, 2021. URL <https://openreview.net/forum?id=PxTIG12RRHS>.

Wang, H., Cao, Y., Huang, Z., Liu, Y., Hu, P., Luo, X., Song, Z., Zhao, W., Liu, J., Sun, J., et al. Recent advances on machine learning for computational fluid dynamics: A survey. *arXiv preprint arXiv:2408.12171*, 2024.

Wang, Z., Bovik, A. C., Sheikh, H. R., and Simoncelli, E. P. Image quality assessment: From error visibility to structural similarity. *IEEE Transactions on Image Processing*, 13(4):600–612, 2004. doi: 10.1109/TIP.2003.819861.

Yang, G. and Sommer, S. A denoising diffusion model for fluid field prediction, 2023. URL <https://arxiv.org/abs/2301.11661>.

Yang, L. and Hong, S. Unsupervised time-series representation learning with iterative bilinear temporal-spectral fusion. 07 2022.

Yu, S., Tack, J., Mo, S., Kim, H., Kim, J., Ha, J.-W., and Shin, J. Generating videos with dynamics-aware implicit generative adversarial networks. In *International Conference on Learning Representations*, 2022.

Yue, Z., Wang, J., and Loy, C. C. Resshift: Efficient diffusion model for image super-resolution by residual shifting, 2023. URL <https://arxiv.org/abs/2307.12348>.

Zhang, R., Isola, P., Efros, A. A., Shechtman, E., and Wang, O. The unreasonable effectiveness of deep features as a perceptual metric. In *Proceedings of the IEEE Conference on Computer Vision and Pattern Recognition (CVPR)*, pp. 586–595, 2018.

Zhang, Y., Zhang, D., and Jiang, H. Review of challenges and opportunities in turbulence modeling: A comparative analysis of data-driven machine learning approaches. *Journal of Marine Science and Engineering*, 11(7):1440, 2023.

Zhu, Y., Zhang, K., Liang, J., Cao, J., Wen, B., Timofte, R., and Gool, L. V. Denoising diffusion models for plug-and-play image restoration. In *IEEE Conference on Computer Vision and Pattern Recognition Workshops (NTIRE)*, 2023.

A Limitations

Although the proposed diffusion framework achieves a significant speedup compared to high-fidelity solvers, it remains relatively slow compared to direct mapping models. Future work could explore recent advancements in accelerating diffusion sampling, such as Lu et al. (2022), to further enhance the efficiency of the reconstruction process.

B Broader Impacts

By enhancing the accuracy of CFD simulations, this approach can significantly reduce the computational costs associated with high-resolution simulations, which are often prohibitively expensive in terms of both time and resources. This has implications for a wide range of industries, including aerospace, automotive design, and environmental engineering, where high-fidelity simulations are essential for optimizing performance, safety, and sustainability. Additionally, by improving the quality of low-resolution CFD data, our work could enable more accessible, efficient research and development processes, allowing smaller organizations and research teams to leverage advanced simulation capabilities.

C Dataset

All datasets are generated using pseudo-spectral solver. The time-stepping method employed is a combination of the Crank-Nicholson scheme and Heun's method. For numerical stability, the solver uses an adaptive time-stepping approach governed by the Courant-Friedrichs-Lowy (CFL) condition. The CFL condition ensures that the time step remains sufficiently small relative to the velocity field and the external forcing, preventing instabilities that can arise from rapid changes in the solution. Additionally, the dealiasing procedure, using the 2/3 rule, removes high-frequency components from the Fourier spectrum, ensuring that non-physical aliasing effects are avoided.

Algorithm 2 Pseudo-spectral Navier-Stokes Solver

```
1: Input: Initial vorticity  $\omega_0$ , forcing  $f$ , Reynolds number  $Re$ , total time  $T$ , timestep  $\Delta t$ , domain size  $L_1, L_2$ , grid size  $s_1, s_2$ , adaptivity flag
2: Output: Vorticity  $\omega$  at time  $T$ 
3: Initialize: Compute wavenumbers, Laplacian, and dealiasing mask
4:
5: while  $t < T$  do
6:   if adaptive then
7:     Compute velocity field  $\mathbf{u} = \nabla^\perp \psi$ 
8:     Update timestep  $\Delta t$  based on CFL
9:   end if
10:  Compute non-linear term in Fourier space
11:  Predictor and corrector steps using Crank-Nicholson + Heun
12:  Apply dealiasing mask
13:  Update time  $t = t + \Delta t$ 
14: end while
15: Return Vorticity  $\omega$ 
```

Taylor Green Vortex The initial vorticity field is based on the analytical solution of the TGV, and to generate different trajectories, we added random perturbations from a Gaussian random field. These perturbations introduce variability to the initial conditions while maintaining the overall vortex structure. No external forcing was applied during the simulation, and the spatial domain is $[0, \frac{3}{2}\pi]^2$ with a fixed Reynolds number of 1000. The simulation used a time step $dt = \frac{1}{32}$, and 100 trajectories were generated each with a total duration of $T = 6$ seconds. The initial vorticity field is based on the analytical solution for the two-dimensional periodic domain. The vorticity field ω is initialized as $\omega = -2U_0 k \sin(kx) \sin(ky)$, where U_0 is the initial velocity amplitude, and k is the wave number that determines the size of the vortices. To introduce variability and generate different trajectories, a Gaussian Random Field is added as a perturbation to the initial vorticity.

Decaying Turbulence The spatial domain is $[0, 1]^2$, with periodic boundary conditions and a fixed Reynolds number of 450. The simulation used a time step $dt = \frac{1}{32}$, and 400 trajectories were generated, each with a total duration of $T = 2$ seconds. The initial conditions for the decaying turbulence dataset are generated by superimposing randomly positioned vortices of varying intensity and size. Each vortex is characterized by a randomly selected core size and maximum rotational velocity, allowing for a diverse range of initial flow structures. The vortices are distributed randomly throughout the domain, and their periodic images are added to ensure the proper enforcement of periodic boundary conditions.

Kolmogorov Flow The initial vorticity field is generated using a Gaussian random field, and the system is subjected to a forcing term of the form $f(\mathbf{x}) = -4 \cos(4x_2) - 0.1\omega(\mathbf{x}, t)$. This forcing drives the flow in the y -direction while introducing a drag force that dissipates energy. The spatial domain is $[0, 2\pi]^2$, with a fixed Reynolds number of 1000. The simulation used a time step $dt = \frac{1}{32}$, and 50 trajectories were generated, each with a total duration of $T = 10$ seconds. The initial vorticity field is produced by sampling from a Gaussian Random Field. As the external forcing continually adds energy to the system, the initially simple vorticity evolves into intricate and turbulent structures. The vorticity is allowed to evolve over a 5-second period, and the final state at the end of this interval is used as the initial condition for our dataset.

McWilliams Flow The phenomenon illustrates the emergence of order from initially disordered turbulent motion, driven by viscous dissipation and the self-organization of the flow. No external forcing is applied during the simulation, allowing for a natural decay and evolution of the turbulence. The spatial domain is $[0, 2\pi]^2$, with periodic boundary conditions and a Reynolds number of 2000, providing a high degree of turbulence. The simulation used a time step $dt = \frac{1}{32}$, and 50 trajectories were generated, each with a total duration of $T = 10$ seconds. The initial vorticity field for the *McWilliams Flow* is generated following the method described by Mcwilliams (1984). The process begins by constructing a Fourier mesh over the spatial domain, where the wavenumbers k_x and k_y are calculated. A scalar wavenumber function is prescribed, and the ensemble variance is determined to ensure that the energy distribution in Fourier space follows the desired spectral shape. Random Gaussian perturbations are applied to each Fourier component of the stream function, producing a random realization of the vorticity field. To ensure the stream function has a zero mean, a spectral filter is applied, and the field is normalized based on the kinetic energy. Finally, the vorticity field is computed in physical space by taking the inverse Laplacian of the stream function in Fourier space, resulting in a turbulent flow field that evolves naturally without external forcing.

	Kolmogorov Flow	McWilliams Flow	Taylor Green Vortex	Decaying Turbulence
Res.	44.13	6.64	5101.65	212.43

Table 3: Residual of high-fidelity samples for each dataset.

D Experiment Results for Direct Mapping Models

For direct mapping models, we compare against a CNN-based model (Fukami et al., 2019), a GAN-based model (Li & McComb, 2022). Note that we apply 5 steps of gradient descent using the residual to the reconstructed sample to enhance physical consistency. The results are reported in Table 4.

	Metric	CNN	GAN
<i>Taylor Green Vortex</i>	L2	3.66	3.53
	Res.	65410.59	11872.01
<i>Decaying Turbulence</i>	L2	2.69	2.52
	Res.	52661.27	9561.52
<i>Kolmogorov Flow</i>	L2	2.01	2.09
	Res.	2137.63	766.17
<i>McWilliams Flow</i>	L2	1.40	2.04
	Res.	1817.93	645.18
<i>Kolmogorov Flow</i>	L2	3.41	3.11
	Res.	1046.39	412.16
<i>McWilliams Flow</i>	L2	3.13	3.04
	Res.	645.07	393.35
<i>Kolmogorov Flow</i>	L2	2.31	2.20
	Res.	176.55	266.63
<i>McWilliams Flow</i>	L2	1.61	1.92
	Res.	183.89	267.27

Table 4: Quantitative performance comparison over four datasets on L2 and Res. Metrics are reported for both $32 \times 32 \rightarrow 256 \times 256$ (gray) and $64 \times 64 \rightarrow 256 \times 256$ tasks.

E Multi-Scale Evaluation

Table 5: Kolmogorov Flow $4 \times$ Upsampling

Method	HH	HL	LL	LH
DiffPIR	4.3914	9.0811	188.6012	3.6674
DPS	4.3978	9.0713	187.9728	3.6626
ResShift	0.1164	1.6399	13.4812	1.9845
PiRD	0.1093	1.6150	12.9042	1.9455
RSGD	0.0336	0.2134	13.5701	0.4348
Diffusion	0.0279	0.2437	14.0867	0.4011
Cond Diff	0.0294	0.2476	14.1269	0.4137
SG-Diff	0.0263	0.2103	12.0338	0.3216

Table 6: Kolmogorov Flow $8 \times$ Upsampling

Method	HH	HL	LL	LH
DiffPIR	4.3914	9.0811	188.6012	3.6674
DPS	4.3914	9.0795	188.0532	3.6646
ResShift	0.0722	1.8942	39.4973	2.1263
PiRD	0.0649	1.8410	37.2648	2.0639
RSGD	0.0346	0.2947	40.0763	0.4904
Diffusion	0.0382	0.2935	41.8237	0.4429
Cond Diff	0.0344	0.2903	42.9040	0.4445
SG-Diff	0.0312	0.2616	33.8086	0.3798

Table 7: McWilliams Flow 4× Upsampling

Method	HH	HL	LL	LH
DiffPIR	0.4226	1.1473	75.6783	0.5940
DPS	0.4225	1.1465	75.4513	0.5932
ResShift	0.0523	0.9234	6.8736	0.8362
PiRD	0.0516	0.9271	6.8646	0.8350
RSGD	0.0203	0.2155	6.6627	0.1959
Diffusion	0.0182	0.2108	6.7780	0.1834
Cond Diff	0.0167	0.2229	6.8123	0.1944
SG-Diff	0.0141	0.1642	6.2937	0.1452

Table 8: McWilliams Flow 8× Upsampling

Method	HH	HL	LL	LH
DiffPIR	0.4182	1.1362	75.4749	0.6381
DPS	0.4225	1.1468	75.4864	0.5934
ResShift	0.0320	0.9873	19.3344	0.9170
PiRD	0.0321	0.9917	19.4258	0.9253
RSGD	0.0152	0.2288	23.2287	0.1983
Diffusion	0.0152	0.2287	20.9631	0.2027
Cond Diff	0.0151	0.2353	21.1752	0.2085
SG-Diff	0.0145	0.1920	17.4284	0.1708

Table 9: Decaying Turbulence 4× Upsampling

Method	HH	HL	LL	LH
DiffPIR	5.9452	9.0297	35.3487	3.7063
DPS	5.9452	9.0292	35.3019	3.7059
ResShift	0.0504	0.7032	5.1194	0.7208
PiRD	0.0500	0.7140	5.3197	0.7326
RSGD	0.0442	0.0611	7.4907	0.0431
Diffusion	0.0765	0.0995	5.1389	0.0994
Cond Diff	0.0365	0.0510	29.6782	0.0546
SG-Diff	0.0196	0.0264	5.0720	0.0267

Table 10: Decaying Turbulence 8× Upsampling

Method	HH	HL	LL	LH
DiffPIR	5.9592	9.0601	52.0273	3.7367
DPS	5.9592	9.0600	52.0212	3.7366
ResShift	0.0416	1.1680	26.8325	1.2171
PiRD	0.0416	1.1843	26.7621	1.2353
RSGD	0.0425	0.0508	29.0300	0.0896
Diffusion	0.1780	0.2204	25.0249	0.2159
Cond Diff	0.0461	0.0511	34.5407	0.0591
SG-Diff	0.0238	0.0488	24.1640	0.0512

Table 11: Taylor Green Vortex $4\times$ Upsampling

Method	HH	HL	LL	LH
DiffPIR	19.4488	42.9432	127.4038	5.5207
DPS	19.4477	42.9413	127.1114	5.5192
ResShift	0.3451	1.3825	13.0696	1.3727
PiRD	0.3422	1.3822	20.4812	1.3618
RSGD	0.3385	0.5539	27.0561	0.4622
Diffusion	0.1703	0.2959	11.3933	0.2928
Cond Diff	0.2941	0.5003	77.4125	0.4899
SG-Diff	0.1507	0.2928	9.3202	0.2903

Table 12: Taylor Green Vortex $8\times$ Upsampling

Method	HH	HL	LL	LH
DiffPIR	19.4647	42.9816	141.3724	5.5507
DPS	19.4671	42.9863	141.0834	5.5499
ResShift	0.2900	1.9425	44.7676	1.9238
PiRD	0.2811	1.9054	66.0041	1.8890
RSGD	0.0284	0.4015	84.0803	0.3705
Diffusion	0.0998	0.3941	44.8146	0.3727
Cond Diff	0.0174	0.3832	81.7034	0.3772
SG-Diff	0.0172	0.3811	41.5014	0.3704

F Image Similarity Metrics

Although LPIPS is trained on the ImageNet dataset, which consists of natural images, it remains a valuable metric for evaluating perceptual quality in CFD applications. This is because LPIPS leverages features from deep neural networks that are effective at capturing multi-scale patterns, textures, and perceptual similarities, regardless of the specific domain. Fluid dynamics data often have complex structures and turbulent patterns that share characteristics with textures found in natural images, making LPIPS suitable for assessing the fidelity of reconstructed flow fields. Thus, despite being trained on ImageNet, LPIPS can still effectively quantify how well the reconstructed samples retain important perceptual details, making it a robust metric for evaluating the visual quality of CFD reconstructions.

	DiffPIR	DPS	ResShift	PiRD	RSGD	Diff	Cond Diff	SG-Diff
<i>Kolmogorov Flow</i>	0.6607 0.2318	0.6606 0.2148	0.3343 0.1350	0.3657 0.1625	0.2915 0.1233	0.2848 0.1215	0.2869 0.1229	0.2781 0.1097
<i>McWilliams Flow</i>	0.5993 0.2139	0.5993 0.2148	0.3748 0.1747	0.3684 0.1689	0.3511 0.1498	0.3524 0.1457	0.3540 0.1604	0.2936 0.1298
<i>Decaying Turbulence</i>	0.6616 0.6525	0.2148 0.2148	0.2231 0.2514	0.2262 0.2524	0.1639 0.2115	0.4215 0.3608	0.1688 0.2259	0.1397 0.0637
<i>Taylor Green Vortex</i>	0.5785 0.5702	0.2148 0.2148	0.2559 0.3899	0.2881 0.2478	0.2148 0.1813	0.2525 0.1494	0.1750 0.2362	0.1704 0.1339

Table 13: LPIPS scores for each dataset. Metrics are reported for both $32\times 32 \rightarrow 256\times 256$ (grey) and $64\times 64 \rightarrow 256\times 256$ tasks.

The PSNR and SSIM results are reported below:

Kolmogorov Flow				
Model	4x Upsampling		8x Upsampling	
	PSNR	SSIM	PSNR	SSIM
DiffPIR	22.6139	0.0512	21.5010	0.0394
DPS	22.7173	0.0530	22.7461	0.0532
ResShift	24.4684	0.5587	19.1656	0.3099
PiRD	23.4082	0.5378	19.8004	0.3242
RSGD	25.0200	0.6416	20.6228	0.3608
Diffusion	25.4049	0.6487	21.5818	0.4072
Cond Diff	25.2389	0.6456	20.2067	0.3425
SG-Diff	26.1733	0.6781	24.0754	0.4409

McWilliams Flow				
Model	4x Upsampling		8x Upsampling	
	PSNR	SSIM	PSNR	SSIM
DiffPIR	20.7069	0.0426	20.2405	0.0381
DPS	18.5968	0.0257	18.7903	0.0270
ResShift	28.7484	0.5945	20.3056	0.2827
PiRD	25.2076	0.5110	20.2050	0.2784
RSGD	26.5900	0.6088	21.6394	0.3056
Diffusion	29.7101	0.6686	25.2200	0.3884
Cond Diff	29.6757	0.6665	25.1475	0.3823
SG-Diff	30.0540	0.6722	28.1972	0.4643

Taylor Green Vortex				
Model	4x Upsampling		8x Upsampling	
	PSNR	SSIM	PSNR	SSIM
DiffPIR	30.0668	0.7328	20.2300	0.6633
DPS	30.3133	0.7261	23.2857	0.7373
ResShift	30.5201	0.8009	23.7859	0.6162
PiRD	28.3752	0.7028	22.1947	0.4981
RSGD	25.0744	0.7933	20.9531	0.5955
Diffusion	30.7706	0.8438	24.8698	0.6678
Cond Diff	23.2154	0.6767	21.3979	0.5959
SG-Diff	31.5277	0.8713	26.7503	0.7562

Decaying Turbulence				
Model	4x Upsampling		8x Upsampling	
	PSNR	SSIM	PSNR	SSIM
DiffPIR	31.7640	0.5763	30.3585	0.5160
DPS	31.0463	0.5534	30.1307	0.5088
ResShift	29.0554	0.7998	23.6247	0.5798
PiRD	21.2584	0.7215	27.7594	0.6512
RSGD	40.5449	0.9259	35.3302	0.8185
Diffusion	47.2289	0.9571	40.8901	0.8622
Cond Diff	46.0675	0.9138	40.1089	0.8456
SG-Diff	48.0321	0.9601	43.0276	0.9295

G Runtime Comparison

Table 14 presents the time required for the numerical solver to generate a single frame of low- and high-fidelity samples for each dataset. Note that adaptive time stepping with CFL condition is adopted to ensure numerical stability. The high-fidelity data 256×256 are generated using 4096×4096 and then downsampled to 256×256 . All datasets are generated using pseudo spectral solver that run on GPU.

Dataset	256×256	64×64	32×32
<i>Kolmogorov Flow</i>	246.23	0.44	0.04
<i>McWilliams Flow</i>	156.20	1.23	0.12
<i>Decaying Turbulence</i>	151.70	1.01	0.06
<i>Taylor Green Vortex</i>	247.03	1.49	0.22

Table 14: Run time of numerical solver to generate one frame for each dataset across different grid resolutions with a batch size of 10. All times are measured in seconds.

Table 15 shows the time comparison across ML models for reconstructing high-fidelity data from low-fidelity inputs.

Method	$32 \times 32 \rightarrow 256 \times 256$	$64 \times 64 \rightarrow 256 \times 256$
DiffPIR	17.27	17.27
DPS	17.11	17.11
ResShift	3.96	3.96
PiRD	5.15	5.15
RSGD	6.13	3.14
Diff	6.10	3.06
Cond Diff	6.20	3.38
SG-Diff	6.37	3.27

Table 15: Runtime comparison of various methods across different resolution levels using a batch size of 10, with all times measured in seconds.

H Importance Weight Sensitivity Analysis

We present a sensitivity analysis to explore how different hyperparameter settings affect the performance of the Importance Weight Strategy. The importance weight strategy is governed by three main parameters: β (the maximum importance weight), α (the minimum importance weight), and θ (the importance threshold). We adjust these parameters sequentially. The results are summarized in Figure 4.

I Generalization

We observe that SG-Diff generalizes well to low-fidelity data generated with different solver configurations. We conduct evaluations over three generalization settings: time discretization, spatial domain size, and Reynolds number as shown in Table 16. We train SG-Diff on the original *Kolmogorov Flow* dataset, which has timestep $dt = 1/32$, spatial domain size $2\pi \times 2\pi$, and Reynolds number $Re = 1000$. We then directly test these new low-fidelity data on the trained model, without any additional retraining or fine-tuning. We compare the performance against models directly trained on each new configuration.

The results reveal that the pertained SG-Diff performs comparably to trained ones directly on each new configuration. This underscores our model’s strong generalization capabilities across different solver configurations. Such generalization ability is particularly important given the high-level objective is to combine SG-Diff with solvers operating on coarser grids to generate high-fidelity data faster. The generalization ability can be due to the fact that both our *importance weight* mechanism and *residual correction* modules are training-free. They enable our model to locate fine-grained

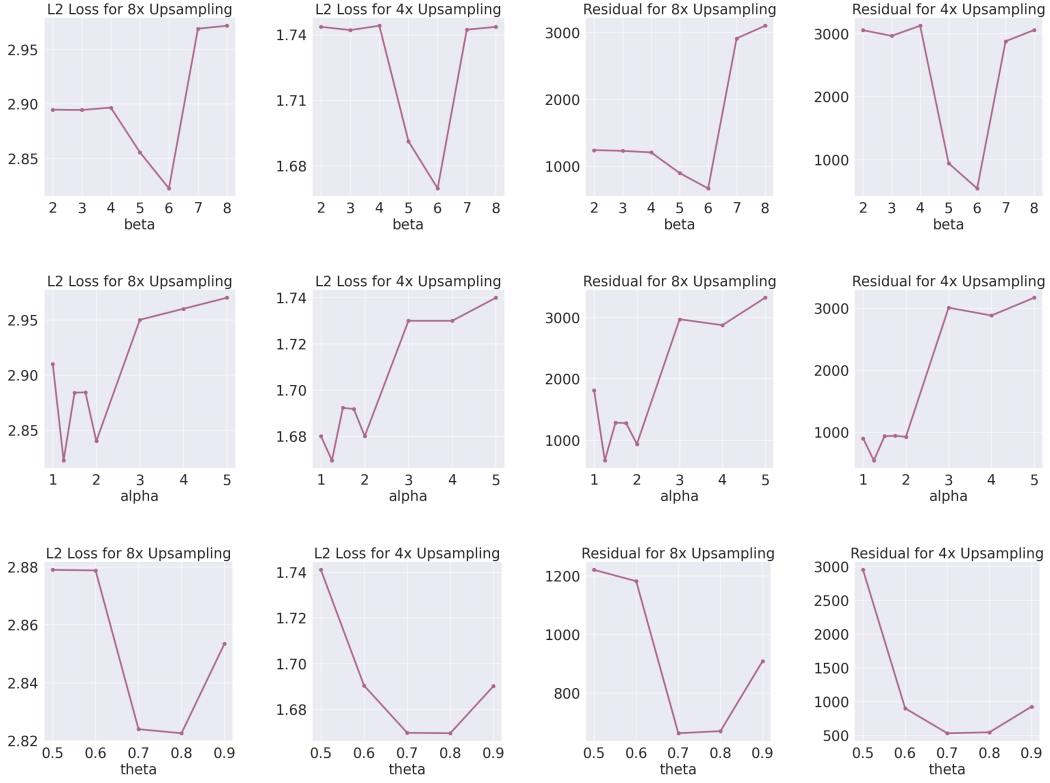


Figure 4: Sensitivity analysis of key parameters for the *Importance Weight*. Experiments are conducted on the *Kolmogorov Flow*. The top row presents the results for the maximum importance weight, β . The middle row displays the results for the minimum importance weight, α , and the bottom row shows the results for the importance threshold, θ . These three hyperparameters were tuned in sequence, and the optimal combination ($\beta = 6$, $\alpha = 1.25$, and $\theta = 0.8$) is selected.

high-fidelity details and adhere to physical laws independent of training data. A similar trend is also observed in $4\times$ upsampling experiments.

Variation	Model	L2	Res.
Time Discretization Variations			
$dt = 1/40$	Trained on Original Data	2.8144	34.29
	Trained on $dt = 1/40$ Data	2.8136	34.52
Spatial Domain Size Variations			
$1\pi \times 1\pi$	Trained on Original Data	1.9045	262.42
	Trained on $1\pi \times 1\pi$ Data	1.7672	190.99
$1.5\pi \times 1.5\pi$	Trained on Original Data	2.3573	80.66
	Trained on $1.5\pi \times 1.5\pi$ Data	2.3028	88.88
Reynolds Number Variations			
$Re = 500$	Trained on Original Data	2.3694	24.11
	Trained on $Re = 500$ Data	2.3542	26.96
$Re = 2000$	Trained on Original Data	3.2957	23.84
	Trained on $Re = 2000$ Data	3.2914	22.48

Table 16: Generalization results on *Kolmogorov Flow* dataset with $32 \times 32 \rightarrow 256 \times 256$ setting.

Table 17: Generalization results on *Kolmogorov Flow* dataset with $64 \times 64 \rightarrow 256 \times 256$ setting.

Variation	Model	L2	Res.
Time Discretization Variations			
$dt = 1/40$	Trained on Original Data	1.6782	31.49
	Trained on $dt = 1/40$ Data	1.6723	30.91
$dt = 1/50$	Trained on Original Data	1.6484	33.49
	Trained on $dt = 1/50$ Data	1.6489	26.66
Spatial Domain Size Variations			
$1\pi \times 1\pi$	Trained on Original Data	1.0255	263.23
	Trained on $1\pi \times 1\pi$ Data	0.9443	207.03
$1.5\pi \times 1.5\pi$	Trained on Original Data	1.3212	84.24
	Trained on $1.5\pi \times 1.5\pi$ Data	1.2918	94.87
Reynolds Number Variations			
$Re = 500$	Trained on Original Data	1.3112	21.57
	Trained on $Re = 500$ Data	1.2998	22.96
$Re = 2000$	Trained on Original Data	1.9647	24.07
	Trained on $Re = 2000$ Data	1.9694	24.22

J Proof of Proposition 3.1

We assume each frame is multivariate gaussian and compare the KL divergence between high-fidelity data added with diffusion noise at t_{guide} and solver generated low-fidelity added with diffusion noise at t_{guide} and KL divergence between high-fidelity data added with diffusion noise at t_{guide} and downsampled low-fidelity data added with diffusion noise at t_{guide} . The low-fidelity data are upsampled uniformly to 256×256 when computing the KL divergence. This also matches the methodology used during inference.

	$D_{\text{KL}}(\tilde{p}_{\mathcal{Y}} \parallel \tilde{p}_{\mathcal{X}})$	$D_{\text{KL}}(\tilde{p}_{\mathcal{Y}} \parallel \tilde{q}_{\mathcal{X}})$
Kolmogorov Flow		
32×32	207.61	173.07
64×64	43.45	36.69
McWilliams Flow		
32×32	56.58	39.75
64×64	12.26	10.36
Decaying Turbulence		
32×32	39.34	33.37
64×64	8.65	7.39
Taylor Green Vortex		
32×32	9225.79	7741.20
64×64	1871.14	1574.79

K Proof of Proposition 3.3

Give the Predictor-Corrector-Advancer SDE solver as follows:

- Predictor $\tilde{x}_0^t = \text{NN}_{\theta}(x_t, t)$
- Corrector $\tilde{x}_0^t = \mathcal{C}(\tilde{x}_0^t)$ if correction is applied else $\bar{x}_0^t = \tilde{x}_0^t$
- Advancer $x_{t-1} = x_t + \left[f(x_t, t) + g^2(t) \frac{x_t - \tilde{x}_0^t - \int_0^t f(x_s, s) ds}{\int_0^t g^2(s) ds} \right] dt + g(t) d\bar{W}$

We can consider the SDE of interest to be

$$dx = \left[f(x, t) + g^2(t) \frac{x_t - \tilde{x}_0^t - \int_0^t f(x_s, s) ds}{\int_0^t g^2(s) ds} \right] dt + g(t) d\bar{W}$$

Define $\bar{f}(x, t) = f(x, t) + g^2(t) \frac{x_t - \tilde{x}_0^t - \int_0^t f(x_s, s) ds}{\int_0^t g^2(s) ds}$ and $\bar{g}(t) = g(t)$.

Assumption K.1. Let $f(x, t)$ and $g(t)$ be the drift function and diffusion coefficient of VP-SDE (Ho et al., 2020). Then, $f(x, t)$ is Lipschitz with respect to x with Lipschitz constant L_f .

Then, if \hat{x}_t denotes the piecewise constant solution, for $0 \leq t \leq T$,

$$\begin{aligned} Z(t) &= \sup_{0 \leq s \leq t} \mathbb{E} [|x_s - \hat{x}_s|^2] \\ &= \sup_{0 \leq s \leq t} \mathbb{E} \left| \int_0^{t_n} \bar{f}(x_u, t_u) - \bar{f}(\hat{x}_u, t_u) \, du + \int_0^{t_n} \bar{g}(t_u) - \bar{g}(t_u) \, dW_u \right. \\ &\quad \left. + \int_{t_n}^s \bar{f}(\hat{x}_u, t_u) \, du + \int_{t_n}^s \bar{g}(t_u) \, dW_u \right|^2 \\ &= \sup_{0 \leq s \leq t} \mathbb{E} \left| \int_0^{t_n} \bar{f}(x_u, t_u) - \bar{f}(\hat{x}_u, t_u) \, du + \int_{t_n}^s \bar{f}(\hat{x}_u, t_u) \, du + \int_{t_n}^s \bar{g}(t_u) \, dW_u \right|^2 \end{aligned}$$

By Cauchy Schwarz inequality

$$\leq 3 \sup_{0 \leq s \leq t} \mathbb{E} \left| \int_0^{t_n} \bar{f}(x_u, t_u) - \bar{f}(\hat{x}_u, t_u) \, du \right|^2 + \left| \int_{t_n}^s \bar{f}(\hat{x}_u, t_u) \, du \right|^2 + \left| \int_{t_n}^s \bar{g}(t_u) \, dW_u \right|^2$$

By linearity of expectation, Ito's isometry, and Cauchy Schwarz inequality,

$$\begin{aligned} &\leq 3 \sup_{0 \leq s \leq t} T \mathbb{E} \left[\int_0^{t_n} |\bar{f}(x_u, t_u) - \bar{f}(\hat{x}_u, t_u)|^2 \, du \right] \\ &\quad + \Delta t \mathbb{E} \left[\left| \int_{t_n}^s |\bar{f}(\hat{x}_u, t_u)|^2 \, du \right| \right] + \mathbb{E} \left[\int_{t_n}^s |\bar{g}(t_u)|^2 \, du \right] \end{aligned}$$

Note that in $\bar{f}(x_t, t) = f(x_t, t) + g^2(t) \frac{x_t - \bar{x}_0^t - \int_0^t f(x_s, s) \, ds}{\int_0^t g^2(s) \, ds}$, $f(x_t, t)$ is Lipchitz with respect to x_t by construction. $g^2(t)$, $\int_0^t f(x_s, s) \, ds$, and $\int_0^t g^2(s) \, ds$ are constant with respect to x_t .

Assumption K.2. The predictor $\hat{x}_0^t = \text{NN}_\theta(x_t, t)$ is Lipschitz with Lipschitz constant L_{NN} .

The Lipschitz assumption for the predictor is simply requiring the gradient with respect to the input x_t to be bounded. This is a necessary condition for training NN_θ .

Assumption K.3. Let \mathcal{R} be the PDE residual. Then, $\nabla \mathcal{R}(x)$ and $\nabla^2 \mathcal{R}(x)$ are bounded within the domain of interest. Further, $\nabla \mathcal{R}(x)$ is Lipschitz with respect to x with Lipschitz constant $L_{\mathcal{R}}$.

The corrector $\bar{x}_0^t = \mathcal{C}(\tilde{x}_0^t)$ involves M steps of gradient descent using the gradient of the PDE residual. In the context of PDEs—particularly for the turbulent Navier–Stokes equations—this assumption may not hold due to the inherently irregular and multi-scale nature of turbulent flows. Despite this, Shu et al. (2023) incorporate $\nabla \mathcal{R}(x)$ as an input to the denoiser, a procedure that necessitates the boundedness of both $\nabla \mathcal{R}(x)$ and $\nabla^2 \mathcal{R}(x)$ to ensure stable gradient propagation. Consequently, we adopt the assumption that $\nabla \mathcal{R}(x)$ and $\nabla^2 \mathcal{R}(x)$ are bounded within the domain of interest.

For the Adam gradient descent, $m_{t+1} = \beta_1 m_t + (1 - \beta_1) \nabla \mathcal{R}(x_t)$ and $v_{t+1} = \beta_2 v_t + (1 - \beta_2) (\nabla \mathcal{R}(x_t))^2$. The update rule can be written as $x_{t+1} = x_t - \eta Q(m_{t+1}, v_{t+1})$ with $Q(m, v) = \frac{m}{\sqrt{v} + \epsilon}$.

$$\frac{\partial Q}{\partial \nabla \mathcal{R}} = \frac{\frac{\partial m}{\partial \nabla \mathcal{R}} (\sqrt{v} + \epsilon) + m \frac{1}{2} v^{-1/2} \frac{\partial v}{\partial \nabla \mathcal{R}}}{(\sqrt{v} + \epsilon)^2}$$

Using the boundedness of $\nabla \mathcal{R}$ and the Adam parameters, Q is Lipschitz with respect to $\partial \nabla \mathcal{R}$ and assume the Lipschitz constant is L_Q . Then, Q is Lipschitz with respect to x with Lipschitz constant $L_Q L_{\mathcal{R}}$. As a result, the one step gradient descent $\bar{T}(x) = x - \eta Q(x)$ has Lipschitz constant $1 + \eta L_Q L_{\mathcal{R}}$. By induction, M steps of gradient descent has Lipschitz constant $(1 + \eta L_Q L_{\mathcal{R}})^M$.

As a result, The corrector can also be considered as Lipchitz with Lipchitz constant $L_{\bar{f}} = L_f + \frac{|\sup_{0 \leq s \leq T} g^2(s)|}{|\sup_{0 \leq s \leq T} \int_0^s g^2(s)|} (1 + (1 + \eta L_Q L_{\mathcal{R}})^M L_{\text{NN}})$ if correction is applied and $\hat{L}_{\bar{f}} = L_f + \frac{|\sup_{0 \leq s \leq T} g^2(s)|}{|\sup_{0 \leq s \leq T} \int_0^s g^2(s)|} (1 + L_{\text{NN}})$ otherwise. Note that since $(1 + \eta L_Q L_{\mathcal{R}})^M > 1$, $L_{\bar{f}} > \hat{L}_{\bar{f}}$.

Let $A \cup B = [0, t_{ns}]$ and $A \cap B = \emptyset$. Let A denotes the set where correction is applied and B denotes the set where correction is not applied. Then,

$$\begin{aligned} & \int_0^{t_{ns}} |\bar{f}(x_u, t_u) - \bar{f}(\hat{x}_u, t_u)|^2 du \\ &= \int_A |\bar{f}(x_u, t_u) - \bar{f}(\hat{x}_u, t_u)|^2 du + \int_B |\bar{f}(x_u, t_u) - \bar{f}(\hat{x}_u, t_u)|^2 du \\ &\leq L_{\bar{f}} \int_A |x_u - \hat{x}_u|^2 du + \hat{L}_{\bar{f}} \int_B |x_u - \hat{x}_u|^2 du \end{aligned}$$

Define $\alpha = \frac{\int_A |x_u - \hat{x}_u|^2 du}{\int_0^{t_{ns}} |x_u - \hat{x}_u|^2 du} \propto |A|$. Then, $1 - \alpha = \frac{\int_B |x_u - \hat{x}_u|^2 du}{\int_0^{t_{ns}} |x_u - \hat{x}_u|^2 du} \propto |B|$. We have,

$$\leq (\alpha L_{\bar{f}} + (1 - \alpha) \hat{L}_{\bar{f}}) \int_0^{t_{ns}} |x_u - \hat{x}_u|^2 du$$

Then we have

$$\begin{aligned} & \leq 3 \sup_{0 \leq s \leq t} (\alpha L_{\bar{f}} + (1 - \alpha) \hat{L}_{\bar{f}})^2 T \mathbb{E} \left[\int_0^{t_{ns}} |x_u - \hat{x}_u|^2 du \right] \\ &+ \Delta t \mathbb{E} \left[\int_{t_{ns}}^s |\bar{f}(\hat{x}_u, t_u)|^2 du \right] + \mathbb{E} \left[\int_{t_{ns}}^s |\bar{g}(t_u)|^2 dW_u \right] \\ &\leq 3 \sup_{0 \leq s \leq t} \left((\alpha L_{\bar{f}} + (1 - \alpha) \hat{L}_{\bar{f}})^2 T \int_0^{t_{ns}} Z(u) du + \Delta t \mathbb{E} \left[\int_{t_{ns}}^s |\bar{f}(\hat{x}_u, t_u)|^2 du \right] + C \right) \end{aligned}$$

where $C \Delta t = \mathbb{E} \left[\int_{t_{ns}}^s |\bar{g}(t_u)|^2 dW_u \right]$. The Lipchitz condition of $\bar{f}(x, t)$ implies the linear growth condition. There exists K_f such that $|\bar{f}(x, t)| \leq K_f(1 + |x|)$.

$$\begin{aligned} & \leq 3 \sup_{0 \leq s \leq t} (\alpha L_{\bar{f}} + (1 - \alpha) \hat{L}_{\bar{f}})^2 T \int_0^{t_{ns}} Z(u) du + K_f^2 \Delta t \mathbb{E} \left[\int_{t_{ns}}^s |(1 + |x_u|)|^2 du \right] + C \Delta t \\ &\leq 3 \sup_{0 \leq s \leq t} (\alpha L_{\bar{f}} + (1 - \alpha) \hat{L}_{\bar{f}})^2 T \int_0^{t_{ns}} Z(u) du + \Delta t \left[K_f \left(\Delta t + \int_{t_{ns}}^s \mathbb{E} [|x_u|^2] \right) + C \right] \\ &\leq 3 \left((\alpha L_{\bar{f}} + (1 - \alpha) \hat{L}_{\bar{f}})^2 T \int_0^{t_{ns}} Z(u) du + \Delta t \left[K_f^2 \Delta t \left(1 + \sup_{0 \leq t \leq T} \mathbb{E} [|x_t|^2] \right) + C \right] \right) \end{aligned}$$

As a condition for the existence of strong solution, we assume $\sup_{0 \leq t \leq T} \mathbb{E} [|x_t|^2] \leq D$. Then,

$$\leq 3 \left((\alpha L_{\bar{f}} + (1 - \alpha) \hat{L}_{\bar{f}})^2 T \int_0^{t_{ns}} Z(u) du + \Delta t \left[K_f^2 \Delta t \left(1 + \sup_{0 \leq t \leq T} \mathbb{E} [|x_t|^2] \right) + C \right] \right)$$

By Grönwall's inequality,

$$\begin{aligned} Z(T) &= \sup_{0 \leq s \leq T} \mathbb{E} [|x_s - \hat{x}_s|^2] \\ &\leq \Delta t [K_f^2 \Delta t (1 + D) + C] \exp(3(\alpha L_{\bar{f}} + (1 - \alpha) \hat{L}_{\bar{f}})^2 T^2) \end{aligned}$$

Now, notice that

$$\begin{aligned} \alpha &= \frac{\int_A |x_u - \hat{x}_u|^2 du}{\int_0^{t_{ns}} |x_u - \hat{x}_u|^2 du} \\ &\leq \frac{|A| \sup_{0 \leq u \leq t_{ns}} |x_u - \hat{x}_u|^2}{t_{ns} \inf_{0 \leq u \leq t_{ns}} |x_u - \hat{x}_u|^2} = c_1 |A| \end{aligned}$$

Additionally,

$$\begin{aligned}\alpha &= \frac{\int_A |x_u - \hat{x}_u|^2 du}{\int_0^{t_{n_s}} |x_u - \hat{x}_u|^2 du} \\ &\geq \frac{|A| \inf_{0 \leq u \leq t_{n_s}} |x_u - \hat{x}_u|^2}{t_{n_s} \sup_{0 \leq u \leq t_{n_s}} |x_u - \hat{x}_u|^2} = c_2 |A|\end{aligned}$$

Thus, $\alpha = O(|A|)$ and $\alpha^2 = O(|A|^2)$. Next, we notice that

$$\begin{aligned}L_{\bar{f}} &= \hat{L}_{\bar{f}} + \Delta L \\ \Delta L &= \frac{|\sup_{0 \leq s \leq T} g^2(s)|}{|\sup_{0 \leq s \leq T} \int_0^s g^2(s) ds|} (1 + (1 + \eta L_Q L_{\mathcal{R}})^M L_{\text{NN}}) + (L_f - \hat{L}_{\bar{f}})\end{aligned}$$

Thus,

$$\Delta L = O((1 + \eta L_Q L_{\mathcal{R}})^M)$$

Plug in ΔL into $\Lambda = \alpha L_{\bar{f}} + (1 - \alpha) \hat{L}_{\bar{f}}$. We get

$$\begin{aligned}\Lambda &= \hat{L}_{\bar{f}} + \alpha \Delta L \\ \Lambda^2 &= \hat{L}_{\bar{f}}^2 + 2\alpha \hat{L}_{\bar{f}} \Delta L + \alpha^2 \Delta L^2 \\ \Lambda^2 &\leq c_3 \alpha^2 \Delta L^2 = O(|A|^2 (1 + \eta L_Q L_{\mathcal{R}})^{2M})\end{aligned}$$

Thus,

$$\begin{aligned}Z(T) &= \sup_{0 \leq s \leq T} \mathbb{E} [|x_s - \hat{x}_s|^2] \\ &= O(\Delta t \exp(O(|A|^2 (1 + \eta L_Q L_{\mathcal{R}})^{2M})))\end{aligned}$$

L Hardware Specification

We implement all models in PyTorch. All experiments are run on servers/workstations with the following configuration:

- 80 CPUs, 503G Mem, 8 x NVIDIA V100 GPUs.
- 48 CPUs, 220G Mem, 8 x NVIDIA TITAN Xp GPUs.
- 96 CPUs, 1.0T Mem, 8 x NVIDIA A100 GPUs.
- 64 CPUs, 1.0T Mem, 8 x NVIDIA RTX A6000 GPUs.
- 224 CPUs, 1.5T Mem, 8 x NVIDIA L40S GPUs.

NeurIPS Paper Checklist

1. Claims

Question: Do the main claims made in the abstract and introduction accurately reflect the paper's contributions and scope?

Answer: [\[Yes\]](#)

Justification: The claims made in abstract and introduction clearly match our theoretical and empirical results.

Guidelines:

- The answer NA means that the abstract and introduction do not include the claims made in the paper.
- The abstract and/or introduction should clearly state the claims made, including the contributions made in the paper and important assumptions and limitations. A No or NA answer to this question will not be perceived well by the reviewers.
- The claims made should match theoretical and experimental results, and reflect how much the results can be expected to generalize to other settings.
- It is fine to include aspirational goals as motivation as long as it is clear that these goals are not attained by the paper.

2. Limitations

Question: Does the paper discuss the limitations of the work performed by the authors?

Answer: [\[Yes\]](#)

Justification: It is provided in the Appendix and Conclusion.

Guidelines:

- The answer NA means that the paper has no limitation while the answer No means that the paper has limitations, but those are not discussed in the paper.
- The authors are encouraged to create a separate "Limitations" section in their paper.
- The paper should point out any strong assumptions and how robust the results are to violations of these assumptions (e.g., independence assumptions, noiseless settings, model well-specification, asymptotic approximations only holding locally). The authors should reflect on how these assumptions might be violated in practice and what the implications would be.
- The authors should reflect on the scope of the claims made, e.g., if the approach was only tested on a few datasets or with a few runs. In general, empirical results often depend on implicit assumptions, which should be articulated.
- The authors should reflect on the factors that influence the performance of the approach. For example, a facial recognition algorithm may perform poorly when image resolution is low or images are taken in low lighting. Or a speech-to-text system might not be used reliably to provide closed captions for online lectures because it fails to handle technical jargon.
- The authors should discuss the computational efficiency of the proposed algorithms and how they scale with dataset size.
- If applicable, the authors should discuss possible limitations of their approach to address problems of privacy and fairness.
- While the authors might fear that complete honesty about limitations might be used by reviewers as grounds for rejection, a worse outcome might be that reviewers discover limitations that aren't acknowledged in the paper. The authors should use their best judgment and recognize that individual actions in favor of transparency play an important role in developing norms that preserve the integrity of the community. Reviewers will be specifically instructed to not penalize honesty concerning limitations.

3. Theory assumptions and proofs

Question: For each theoretical result, does the paper provide the full set of assumptions and a complete (and correct) proof?

Answer: [\[Yes\]](#)

Justification: The complete proof is in the Appendix.

Guidelines:

- The answer NA means that the paper does not include theoretical results.
- All the theorems, formulas, and proofs in the paper should be numbered and cross-referenced.
- All assumptions should be clearly stated or referenced in the statement of any theorems.
- The proofs can either appear in the main paper or the supplemental material, but if they appear in the supplemental material, the authors are encouraged to provide a short proof sketch to provide intuition.
- Inversely, any informal proof provided in the core of the paper should be complemented by formal proofs provided in appendix or supplemental material.
- Theorems and Lemmas that the proof relies upon should be properly referenced.

4. Experimental result reproducibility

Question: Does the paper fully disclose all the information needed to reproduce the main experimental results of the paper to the extent that it affects the main claims and/or conclusions of the paper (regardless of whether the code and data are provided or not)?

Answer: **[Yes]**

Justification: All hyperparameters are stated in the Appendix or the main paper.

Guidelines:

- The answer NA means that the paper does not include experiments.
- If the paper includes experiments, a No answer to this question will not be perceived well by the reviewers: Making the paper reproducible is important, regardless of whether the code and data are provided or not.
- If the contribution is a dataset and/or model, the authors should describe the steps taken to make their results reproducible or verifiable.
- Depending on the contribution, reproducibility can be accomplished in various ways. For example, if the contribution is a novel architecture, describing the architecture fully might suffice, or if the contribution is a specific model and empirical evaluation, it may be necessary to either make it possible for others to replicate the model with the same dataset, or provide access to the model. In general, releasing code and data is often one good way to accomplish this, but reproducibility can also be provided via detailed instructions for how to replicate the results, access to a hosted model (e.g., in the case of a large language model), releasing of a model checkpoint, or other means that are appropriate to the research performed.
- While NeurIPS does not require releasing code, the conference does require all submissions to provide some reasonable avenue for reproducibility, which may depend on the nature of the contribution. For example
 - (a) If the contribution is primarily a new algorithm, the paper should make it clear how to reproduce that algorithm.
 - (b) If the contribution is primarily a new model architecture, the paper should describe the architecture clearly and fully.
 - (c) If the contribution is a new model (e.g., a large language model), then there should either be a way to access this model for reproducing the results or a way to reproduce the model (e.g., with an open-source dataset or instructions for how to construct the dataset).
 - (d) We recognize that reproducibility may be tricky in some cases, in which case authors are welcome to describe the particular way they provide for reproducibility. In the case of closed-source models, it may be that access to the model is limited in some way (e.g., to registered users), but it should be possible for other researchers to have some path to reproducing or verifying the results.

5. Open access to data and code

Question: Does the paper provide open access to the data and code, with sufficient instructions to faithfully reproduce the main experimental results, as described in supplemental material?

Answer: [\[Yes\]](#)

Justification: All code and data will be publicly released.

Guidelines:

- The answer NA means that paper does not include experiments requiring code.
- Please see the NeurIPS code and data submission guidelines (<https://nips.cc/public/guides/CodeSubmissionPolicy>) for more details.
- While we encourage the release of code and data, we understand that this might not be possible, so “No” is an acceptable answer. Papers cannot be rejected simply for not including code, unless this is central to the contribution (e.g., for a new open-source benchmark).
- The instructions should contain the exact command and environment needed to run to reproduce the results. See the NeurIPS code and data submission guidelines (<https://nips.cc/public/guides/CodeSubmissionPolicy>) for more details.
- The authors should provide instructions on data access and preparation, including how to access the raw data, preprocessed data, intermediate data, and generated data, etc.
- The authors should provide scripts to reproduce all experimental results for the new proposed method and baselines. If only a subset of experiments are reproducible, they should state which ones are omitted from the script and why.
- At submission time, to preserve anonymity, the authors should release anonymized versions (if applicable).
- Providing as much information as possible in supplemental material (appended to the paper) is recommended, but including URLs to data and code is permitted.

6. Experimental setting/details

Question: Does the paper specify all the training and test details (e.g., data splits, hyper-parameters, how they were chosen, type of optimizer, etc.) necessary to understand the results?

Answer: [\[Yes\]](#)

Justification: They are clearly explained in the Appendix and the main paper.

Guidelines:

- The answer NA means that the paper does not include experiments.
- The experimental setting should be presented in the core of the paper to a level of detail that is necessary to appreciate the results and make sense of them.
- The full details can be provided either with the code, in appendix, or as supplemental material.

7. Experiment statistical significance

Question: Does the paper report error bars suitably and correctly defined or other appropriate information about the statistical significance of the experiments?

Answer: [\[Yes\]](#)

Justification: Statistical significance are considered.

Guidelines:

- The answer NA means that the paper does not include experiments.
- The authors should answer “Yes” if the results are accompanied by error bars, confidence intervals, or statistical significance tests, at least for the experiments that support the main claims of the paper.
- The factors of variability that the error bars are capturing should be clearly stated (for example, train/test split, initialization, random drawing of some parameter, or overall run with given experimental conditions).
- The method for calculating the error bars should be explained (closed form formula, call to a library function, bootstrap, etc.)
- The assumptions made should be given (e.g., Normally distributed errors).
- It should be clear whether the error bar is the standard deviation or the standard error of the mean.

- It is OK to report 1-sigma error bars, but one should state it. The authors should preferably report a 2-sigma error bar than state that they have a 96% CI, if the hypothesis of Normality of errors is not verified.
- For asymmetric distributions, the authors should be careful not to show in tables or figures symmetric error bars that would yield results that are out of range (e.g. negative error rates).
- If error bars are reported in tables or plots, The authors should explain in the text how they were calculated and reference the corresponding figures or tables in the text.

8. Experiments compute resources

Question: For each experiment, does the paper provide sufficient information on the computer resources (type of compute workers, memory, time of execution) needed to reproduce the experiments?

Answer: [\[Yes\]](#)

Justification: The runtime comparison is in the Appendix.

Guidelines:

- The answer NA means that the paper does not include experiments.
- The paper should indicate the type of compute workers CPU or GPU, internal cluster, or cloud provider, including relevant memory and storage.
- The paper should provide the amount of compute required for each of the individual experimental runs as well as estimate the total compute.
- The paper should disclose whether the full research project required more compute than the experiments reported in the paper (e.g., preliminary or failed experiments that didn't make it into the paper).

9. Code of ethics

Question: Does the research conducted in the paper conform, in every respect, with the NeurIPS Code of Ethics <https://neurips.cc/public/EthicsGuidelines>?

Answer: [\[Yes\]](#)

Justification: The work conforms with the NeurIPS Code of Ethics.

Guidelines:

- The answer NA means that the authors have not reviewed the NeurIPS Code of Ethics.
- If the authors answer No, they should explain the special circumstances that require a deviation from the Code of Ethics.
- The authors should make sure to preserve anonymity (e.g., if there is a special consideration due to laws or regulations in their jurisdiction).

10. Broader impacts

Question: Does the paper discuss both potential positive societal impacts and negative societal impacts of the work performed?

Answer: [\[Yes\]](#)

Justification: Broader impacts of this work are discussed in the Appendix.

Guidelines:

- The answer NA means that there is no societal impact of the work performed.
- If the authors answer NA or No, they should explain why their work has no societal impact or why the paper does not address societal impact.
- Examples of negative societal impacts include potential malicious or unintended uses (e.g., disinformation, generating fake profiles, surveillance), fairness considerations (e.g., deployment of technologies that could make decisions that unfairly impact specific groups), privacy considerations, and security considerations.
- The conference expects that many papers will be foundational research and not tied to particular applications, let alone deployments. However, if there is a direct path to any negative applications, the authors should point it out. For example, it is legitimate to point out that an improvement in the quality of generative models could be used to

generate deepfakes for disinformation. On the other hand, it is not needed to point out that a generic algorithm for optimizing neural networks could enable people to train models that generate Deepfakes faster.

- The authors should consider possible harms that could arise when the technology is being used as intended and functioning correctly, harms that could arise when the technology is being used as intended but gives incorrect results, and harms following from (intentional or unintentional) misuse of the technology.
- If there are negative societal impacts, the authors could also discuss possible mitigation strategies (e.g., gated release of models, providing defenses in addition to attacks, mechanisms for monitoring misuse, mechanisms to monitor how a system learns from feedback over time, improving the efficiency and accessibility of ML).

11. Safeguards

Question: Does the paper describe safeguards that have been put in place for responsible release of data or models that have a high risk for misuse (e.g., pretrained language models, image generators, or scraped datasets)?

Answer: [Yes]

Justification: The datasets and code used in this work do not pose any risk.

Guidelines:

- The answer NA means that the paper poses no such risks.
- Released models that have a high risk for misuse or dual-use should be released with necessary safeguards to allow for controlled use of the model, for example by requiring that users adhere to usage guidelines or restrictions to access the model or implementing safety filters.
- Datasets that have been scraped from the Internet could pose safety risks. The authors should describe how they avoided releasing unsafe images.
- We recognize that providing effective safeguards is challenging, and many papers do not require this, but we encourage authors to take this into account and make a best faith effort.

12. Licenses for existing assets

Question: Are the creators or original owners of assets (e.g., code, data, models), used in the paper, properly credited and are the license and terms of use explicitly mentioned and properly respected?

Answer: [Yes]

Justification: They are explicitly mentioned and properly respected.

Guidelines:

- The answer NA means that the paper does not use existing assets.
- The authors should cite the original paper that produced the code package or dataset.
- The authors should state which version of the asset is used and, if possible, include a URL.
- The name of the license (e.g., CC-BY 4.0) should be included for each asset.
- For scraped data from a particular source (e.g., website), the copyright and terms of service of that source should be provided.
- If assets are released, the license, copyright information, and terms of use in the package should be provided. For popular datasets, paperswithcode.com/datasets has curated licenses for some datasets. Their licensing guide can help determine the license of a dataset.
- For existing datasets that are re-packaged, both the original license and the license of the derived asset (if it has changed) should be provided.
- If this information is not available online, the authors are encouraged to reach out to the asset's creators.

13. New assets

Question: Are new assets introduced in the paper well documented and is the documentation provided alongside the assets?

Answer: [Yes]

Justification: All datasets and code will be publicly released.

Guidelines:

- The answer NA means that the paper does not release new assets.
- Researchers should communicate the details of the dataset/code/model as part of their submissions via structured templates. This includes details about training, license, limitations, etc.
- The paper should discuss whether and how consent was obtained from people whose asset is used.
- At submission time, remember to anonymize your assets (if applicable). You can either create an anonymized URL or include an anonymized zip file.

14. **Crowdsourcing and research with human subjects**

Question: For crowdsourcing experiments and research with human subjects, does the paper include the full text of instructions given to participants and screenshots, if applicable, as well as details about compensation (if any)?

Answer: [NA]

Justification: The paper does not involve crowdsourcing nor research with human subjects.

Guidelines:

- The answer NA means that the paper does not involve crowdsourcing nor research with human subjects.
- Including this information in the supplemental material is fine, but if the main contribution of the paper involves human subjects, then as much detail as possible should be included in the main paper.
- According to the NeurIPS Code of Ethics, workers involved in data collection, curation, or other labor should be paid at least the minimum wage in the country of the data collector.

15. **Institutional review board (IRB) approvals or equivalent for research with human subjects**

Question: Does the paper describe potential risks incurred by study participants, whether such risks were disclosed to the subjects, and whether Institutional Review Board (IRB) approvals (or an equivalent approval/review based on the requirements of your country or institution) were obtained?

Answer: [NA]

Justification: The paper does not involve crowdsourcing nor research with human subjects.

Guidelines:

- The answer NA means that the paper does not involve crowdsourcing nor research with human subjects.
- Depending on the country in which research is conducted, IRB approval (or equivalent) may be required for any human subjects research. If you obtained IRB approval, you should clearly state this in the paper.
- We recognize that the procedures for this may vary significantly between institutions and locations, and we expect authors to adhere to the NeurIPS Code of Ethics and the guidelines for their institution.
- For initial submissions, do not include any information that would break anonymity (if applicable), such as the institution conducting the review.

16. **Declaration of LLM usage**

Question: Does the paper describe the usage of LLMs if it is an important, original, or non-standard component of the core methods in this research? Note that if the LLM is used only for writing, editing, or formatting purposes and does not impact the core methodology, scientific rigorosity, or originality of the research, declaration is not required.

Answer: [NA]

Justification: The core method development in this research does not involve LLMs as any important, original, or non-standard components.

Guidelines:

- The answer NA means that the core method development in this research does not involve LLMs as any important, original, or non-standard components.
- Please refer to our LLM policy (<https://neurips.cc/Conferences/2025/LLM>) for what should or should not be described.